Development and performance of a novel single-particle polar nephelometer

新しいエアロゾル光散乱全角度分布同時計測装置の開発と性能

Maho Nakagawa

中川　真秀

Nagoya University

2017

Contents

Abstract

A new polar nephelometer (PN) has been developed to measure simultaneously the scattering angular distributions from 11.7° to 168.3° for individual particles in planes parallel and perpendicular to the polarization of the incident laser beam. Each detection plane had 21 silicon photodiode detectors to detect scattered light at a rate of 100 Hz. Laboratory experiments to validate the performance of the instrument were conducted using nearly mono-disperse spherical particles (polystyrene latex and nigrosine) and non-spherical particles (sodium chloride and soot). The observed scattering angular distributions for individual polystyrene latex particles were in good agreement with the results of simulations based on Mie theory. Complex refractive index values for nigrosine particles were determined by comparing the observed scattering angular distributions with the results of simulations. Clear differences between the measured scattering angular distributions and the results of simulations based on Mie theory assuming spherical particles were observed for sodium chloride particles (mobility diameters of 500 and 700 nm) and propane soot particles (mobility diameters of 300, 500, and 700 nm). These results are reasonably explained by theoretical predictions. We also conducted initial observations of ambient particles in Nagoya city, Japan. Scattering angular distributions for particles with a mobility diameter of 500 nm and an average effective density of 1.4 or 0.3 g/cm^3, which were selected with a combination of differential mobility analyzer and aerosol mass particle analyzer, were measured using the PN. As results, scattering angular distributions for nearly spherical inorganic and organic particles with an average effective density of around 1.4 g/cm^3 were found to be distinguishable from non-spherical particles with an average effective density of around

0.3 g/cm^3. This study has demonstrated that our PN has the potential to distinguish between spherical and non-spherical particles.

Chapter 1

General Introduction

1.1 Importance of aerosols for the earth's radiation balance

Atmospheric particles strongly influence the earth's radiation balance both by scattering and absorbing solar radiation (so-called direct effects) and indirectly by altering cloud formation and properties (Boucher et al. 2013) (Fig. 1.1). Both direct and indirect effects are currently large sources of uncertainty in our understanding of radiative forcing. Direct effects are highly uncertain partly because particle optical properties are influenced by numerous variables, including size, refractive index (RI), shape, morphology, and the mixing state of particles (Moosmüller et al. 2009). The angular distribution of light scattering is an important optical property that contributes to how particles affect the radiation balance in the Earth's atmosphere (Boucher et al. 2013). In addition, knowing the angular distribution of light scattering by individual particles would also be of use in determining the size, shape, and RI of particles (Bohren and Huffman 1983).

1.2 Light scattering by small particles

Light scattering substance (or particle) contains number of negatively charged electrons and positively charged nucleuses. When light (that is, transverse electromagnetic oscillation) pass through the scattering substance, the electrons and nucleus are vibrated due to the electromagnetic force of the light. When an upward electric field is applied to the scattering substance, positive and negative point charges are lined up and down to produce an electric dipole. Once the direction of the electric field is reversed, the direction of electric dipoles is also reversed. When light passes

through the scattering substance, spherical electromagnetic waves are radiated due to the oscillation of the electric dipole. Rayleigh scattering refers to the scattering of light for particle, which is enough small compared to the wavelength of incident light. Mie scattering theory can be used for larger spherical particles with no limitation in particle size, wavelength, and refractive index. Figure 1.2 shows examples of light scattering pattern of submicron spherical particles for incident light at 514.5 nm, calculated using the Mie scattering theory (Hansen and Evans 1980). During the light scattering by particle, interference of scattered light from different electric dipole neighboring each other occurs. As a result, oscillation in the scattering angler distribution can be found, especially for spherical particles (Bohren and Huffman 1983).

1.3 Design and applications of the polar nephelometer (PN)

A variety of polar nephelometers (PN) to measure the angular distribution of light scattering have been developed for atmospheric observations and laboratory experiments. There are three main types of PN design (Barkey et al. 2012).

1.3.1 Goniometer design type

In the first type, scattering angular distributions are measured by rotating a single detector in the scattering plane (Figure 1.3) (Volten et al. 2001). Relatively long measurement times are required to obtain the angular distribution, and the angular distribution for a single particle cannot be measured.

1.3.2 Multi detector type

In the second type, scattering angular distributions are measured by multiple detectors at discrete and fixed angular locations (Figure 1.4) (Wyatt et al. 1988; Barkey et al. 2007). Although the angular resolution of this configuration is typically lower than that of the first type, real time measurements of the scattering angular distribution are

possible. Wyatt et al. (1988) developed a multi-angle light scattering detection instrument (DAWN-A) with 14 fiber-optic detectors placed on a spherical light scattering chamber. This instrument was used to distinguish between spherical and non-spherical particles (Sachweh et al. 1995) and to determine the RI values for mono-disperse spherical particles in the 0.2-2 μm diameter range (Dick et al. 2007) by measuring the polar angular dependence of scattering of circularly polarized light. Barkey et al. (2007) developed a 21 detector PN, in which the polarization of incident light was rotated every 3 s by a solenoid-operated half wave plate to be either parallel or perpendicular to the measurement plane. They used the polar nephelometer to determine the RI values of several aerosols (*e.g.*, Kim and Paulson 2013).

1.3.3 Elliptical mirror type

In addition to these two types, another type of PN using an elliptical mirror and linear array detector have also been reported. In this type, scattered light from one focal point of the elliptical mirror is redirected by the elliptical mirror to a linear array detector placed at the other focal point (Figure 1.5). For example, McCrowey et al. (2013) developed a PN utilizing an elliptical mirror, laser, and charge-couple device (CCD) detector. In this PN, scattering angular distributions and their dependence on the polarization of light source were measured across an angle range of 20°–155° of ensemble of particles by rotating a half wave plate.

1.3.4 Integrating nephelometer type

In addition to these PN, a polar integrated nephelometer, Aurora 4000 (Ecotech), is commercially available. The Aurora 4000 can measure scattering in different angular sectors from any scattering angles between 10° and 90° up to 170°, by varying the

shutter's position, in addition to total scattering coefficients (Chamberlain-Ward and Sharp, 2011).

1.4 The purpose of this article

To our knowledge, however, no instrument has been developed that is capable of real-time measurements of scattering angular distributions and their polarization dependence for single ambient particles. In this study, a new PN has been developed to measure angular distributions of light scattering from single particles. Uniquely, the instrument combines simultaneous detection in planes both parallel and perpendicular to the polarization of the incident laser beam. The performance of the instrument was characterized in laboratory tests with a variety of particles and its applicability for characterizing ambient particles was demonstrated.

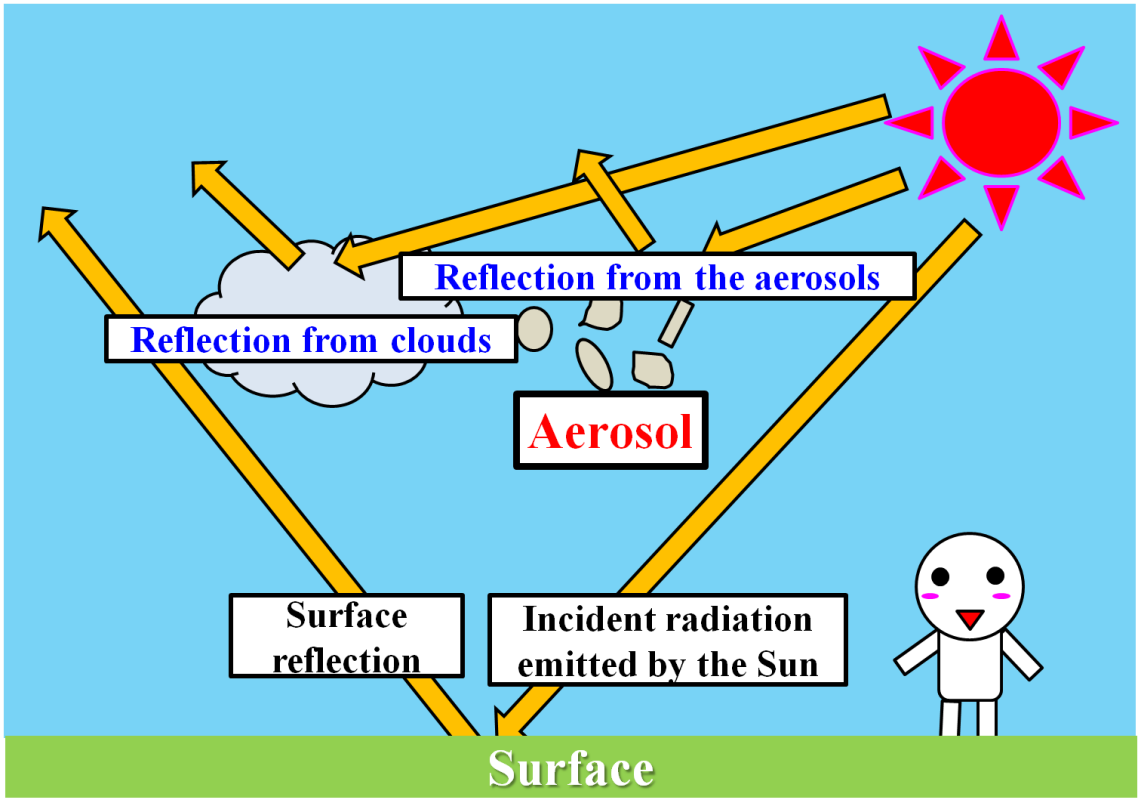

Figure 1.1. Schematic diagram showing the radiative mechanisms associated with aerosols and cloud effects. The small gray circles and the arrowed lines show aerosol particles and the incident and reflected solar radiation, respectably. Aerosols affect the Earth's radiation field directly by scattering and absorbing properties. This direct effect of aerosols may lead to significant implications on the climate.

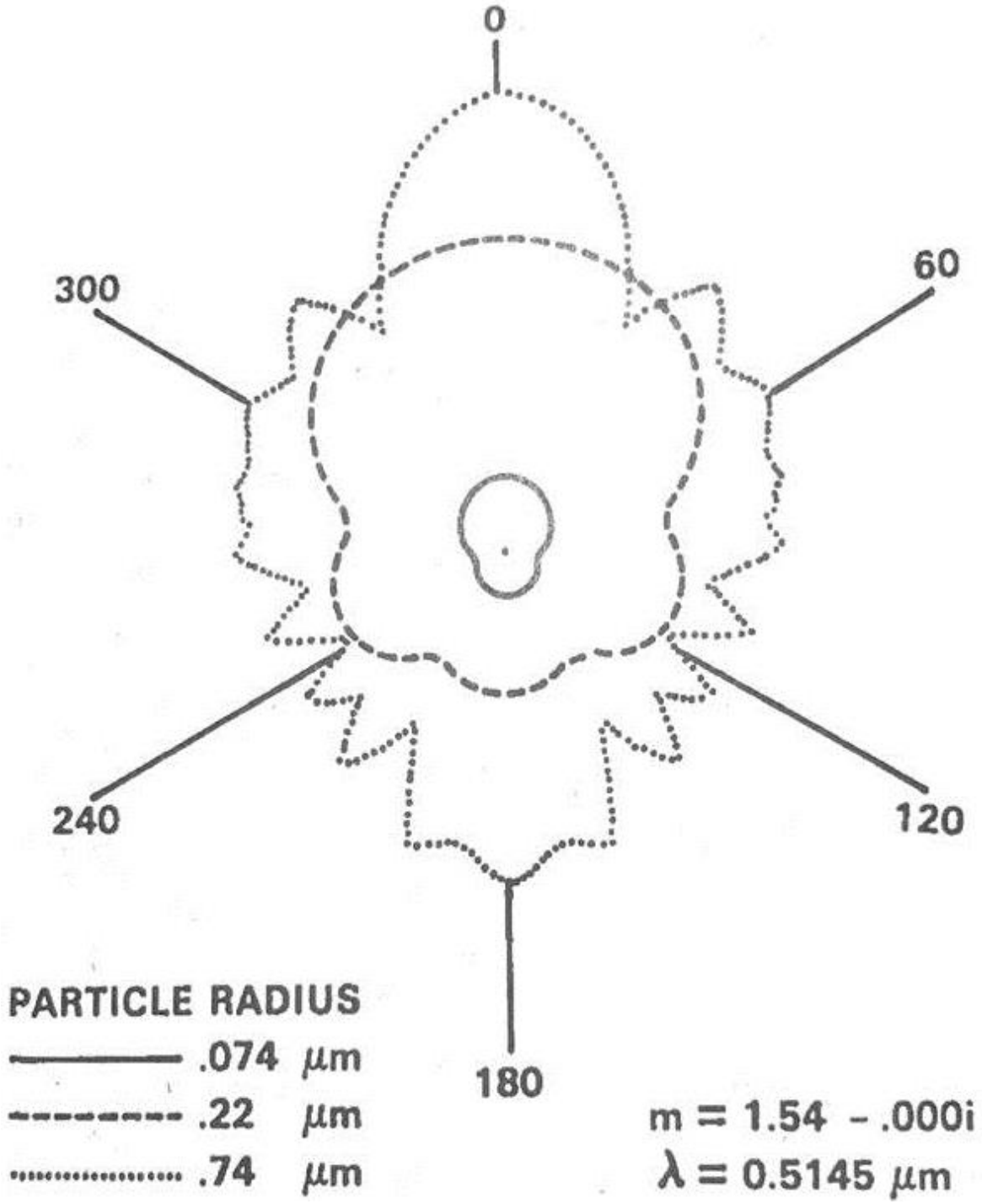

Figure 1.2. The angular distribution of light scattering for spherical submicron particles. (Hansen and Evans 1980)

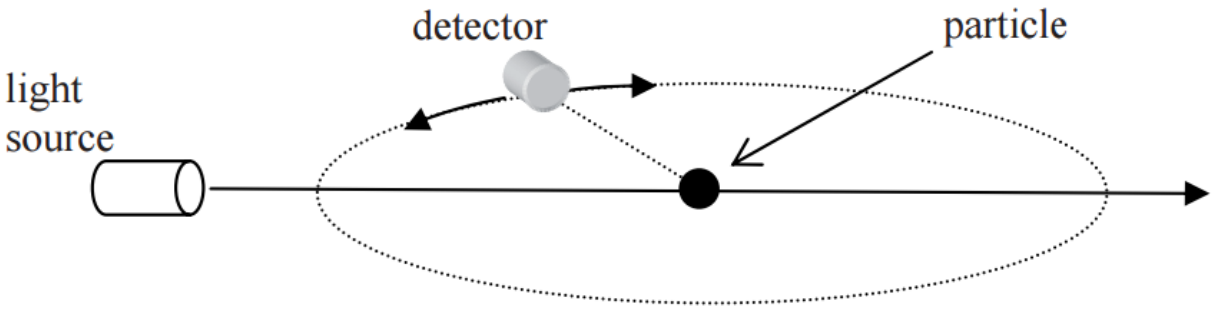

Figure 1.3. Diagram of the Goniometer design type image showing rotating a single detector are required to obtain the angular distribution. (Barkey et al. 2012)

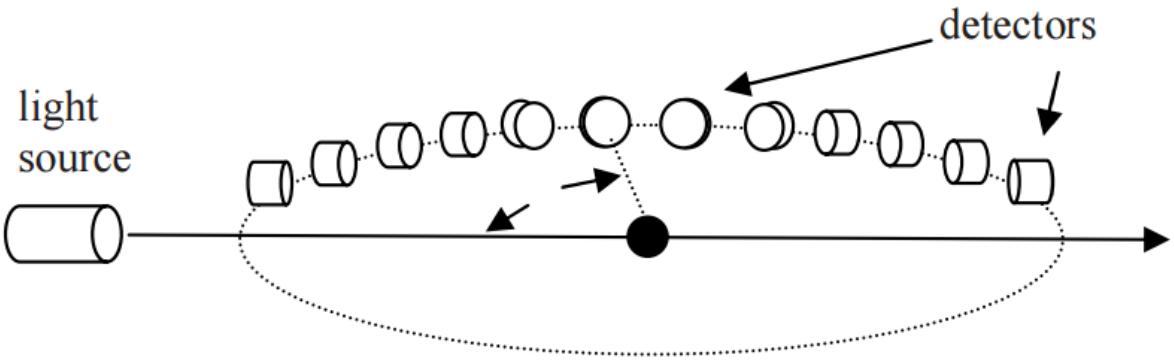

Figure 1.4. Diagram of the multi detector type image showing the configuration of several detectors are fixed at discrete angular positions. (Barkey et al. 2012)

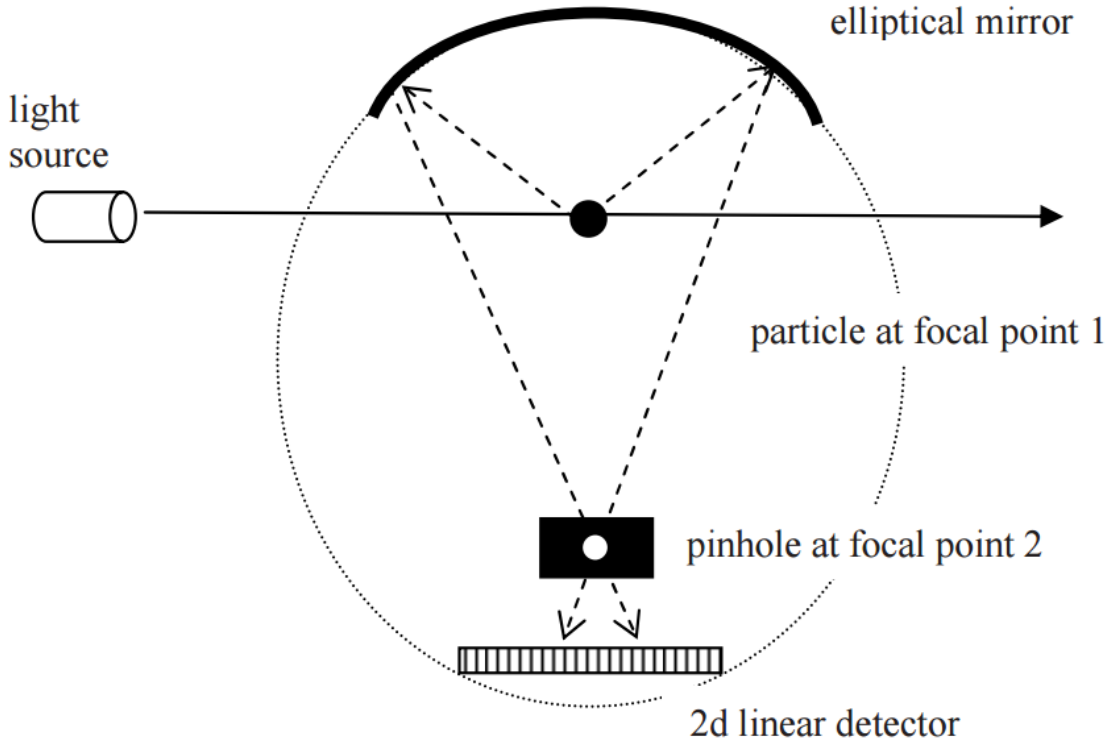

Figure 1.5. Diagram of the elliptical mirror type image showing the scattered light from one focal point of the elliptical mirror is redirected by the elliptical mirror to a linear array detector placed at the other focal point. (Barkey et al. 2012)

Chapter 2

Experimental

2.1 Design of the polar nephelometer

Figure 2.1 and 2.2 show a schematic representation of the new PN. The light source was a linearly polarized frequency doubled 532 nm Nd:YAG laser (Chungchun New Industries, Optoelectronics Technology, Jilin, China, 300 mW) operating in continuous-wave mode. Particles in an aerosol stream were illuminated by the laser beam at the center of the two detection planes, and the transmitted laser light terminated in a beam dump (Figure 2.3). The detection planes were oriented parallel and perpendicular to the polarization of the laser beam. A lens (Edmund Optics, 49783INK) and pinhole (0.5 mm) in front of the nephelometer collimated the laser output into a narrow beam (Figure 2.4).

The laser beam intersected a stream of aerosol particles introduced in a sheath flow using a double pipe with external diameters of 9 and 30 mm. The size of particle inlet pipe was chosen considering angular resolutions of the detectors and sample flow rate. The interaction area is estimated from the diameter of the laser beam (~1 mm) and the particle inlet pipe to be ~0.09 cm^2, assuming that particles remain within the 9 mm diameter as they pass through the beam. The respective flow rates of sample and filtered sheath air were maintained at 0.1 and 0.3 standard liters per minute (slm) using mass flow controllers (Horiba STEC, SEC-E40MK3). A CCD camera (Imaging Source, DMK 21BU04) was placed on the side of the chamber to check the laser alignment and interaction areas (Figure 2.5).

Each detection plane had 21 silicon photodiode detectors (Hamamatsu, S8745-01)

for measuring angular scattering distributions from 11.7° to 168.3°, giving an angular resolution of 7.8° (Figure 2.6). The distance from the detector to the beam-particle interaction spot was 96 mm and the photoelectric surface diameters of the detectors were 3 mm. To avoid detector saturation, especially at forward and backward angles close to 0° and 180°, 50 mm long cylindrical apertures with inner diameters of 4, 2, 1, or 0.5 mm were placed between the scattering point and the various detectors (Table 1). The solid angle for each detector calculated assuming a point scattering source was also listed in Table 1.

Angular distributions of scattering intensity by single particles were acquired at 100 Hz simultaneously in both detection planes. Scattering signals digitized using a 16-bit AD converter (National Instruments, NI-6225), and stored in a personal computer. The instrument was enclosed in a chamber, 36 cm × 43 cm × 22 cm (33 L), and surfaces inside the chamber including tubes, apertures, and housing of detectors were painted black to reduce stray light (Figure 2.7).

2.2 Experimental setup

Figure 2.8 shows a schematic diagram of the sample handling system, which consists of subsystems for particle generation, sizing and mass selection. Nearly-monodisperse particles were prepared using the same procedures as in our previous studies (Nakayama et al. 2010; 2015). Nearly mono-disperse particles were selected using a combination of a differential mobility analyzer (DMA, TSI, 3080) and aerosol particle mass analyzer (APM, Kanomax, Model 3601) before introduction into the PN. The DMA separated particles into different mobility diameters based on the balance between electrostatic and drag forces. The ratio of the sample and sheath flows of the DMA was held constant

at a value of 0.10. The APM separated particles into different masses based on a balance between electrostatic and centrifugal forces. In this study, the APM was used to remove multi-charged particles that were passed through the DMA. The λ parameter which characterizes the classification performance of the APM (Tajima et al. 2011) was fixed at 0.50. Before the scattering angular distribution measurements on these particles, the PN chamber was filled with filtered air to avoid interferences from residual particles. All the experiments were conducted under room temperature and atmospheric pressure conditions.

2.3 Temporal evolution of scattering signal

Fig. 2.9 (a) and (b) show examples of temporal variations of the light intensities detected by two photodiode detector placed at 11.7° on the planes (a) parallel and (b) perpendicular to the laser polarization, respectively, when polystyrene latex (PSL) particles with a mobility diameter of 707 nm were introduced into the instrument. As can be seen in Fig. 2.9, light scattering of single particles can be distinguished and each particle typically passed through the laser beam within 0.1 sec. The detectable size range of single PSL particles of the PN was approximately from 300 to 900 nm in diameter.

2.4 The angular distributions of Rayleigh scattering for pure gases

To validate the linearity of each photodiode, angular distributions of Rayleigh scattering for pure CO_2 and HFC-134a gases were measured. The difference in scattering intensity between pure HFC-134a and air at each scattering angle was compared to that between pure CO_2 and air. The ratio of the difference ($\pm 1\sigma$) for the detectors with an aperture diameter of 4 mm was 3.81 ± 0.12, which is consistent with

the literature value, 3.88 (Air Resource Specialists, Inc. 2005).

2.5 Simulation of scattering angular distributions

Scattering angular distributions of homogeneous spherical particles can be calculated using Lorenz–Mie theory. In practice, the beam-particle interaction volume and the photoelectric surface diameter of the detectors have a finite size, while the detection efficiency and angular resolution vary according to position and aperture size for each detector. These contributions must be taken into account when comparing calculated scattering distributions with measurements.

Fig. 2.10 shows the optical geometry of our PN. The fraction of scattered photons entering each detector was calculated by combining the Lorenz–Mie theory and a Monte Carlo simulation. Scattering angular distributions of single particles were calculated based on Lorenz–Mie theory using a code of BHMIE (Bohren and Huffman 1983), assuming particle size and RI.

The Monte Carlo simulation was used to calculate the fraction of scattered photons entering each detector (Krauth 2006). The simulation assumed that every particle at a random position between $-L_{max}$ to L_{max} along the laser beam path scatters the laser light with local zenith (θ) and azimuth (ϕ) scattering angles. The L_{max} was assumed to be 4.5 mm and the cross-section of laser beam was assumed to be infinitely small. It is also assumed that no refraction occurred at apertures and detectors. The fraction of photons entering each detector was determined by calculating more than 10^6 scattering traces with random local zenith and azimuth scattering angles and the results were shown in Fig. 2.11. The minimum fraction was observed for the detector for side scattering at θ = 90.0° among the detectors with the same inner diameter of cylindrical apertures. The

even smaller fractions were observed for detectors for forward and backward scattering because of the smaller inner diameter of the apertures.

The angular resolution of the detector for forward scattering (*e.g.*, ±1.5° at θ = 11.5°) was higher than that for side scattering (*e.g.*, ±3.0° at θ = 90.0°). By combining the results of the Lorenz–Mie theory and the Monte Carlo calculation, the effective scattering angular distributions (after accounting for the detection efficiency and angular resolution of each detector) were calculated and then compared with measured distributions.

Although beyond the scope of the present study, comparisons of observed angular distributions with results of non-spherical calculations such T-matrix methods (*e.g.*, Mackowski 2012) and discrete dipole approximation (*e.g.*, Yurkin and Hoekstra 2007) would be valuable for detailed understanding of scattering angular distributions of non-spherical particles.

Table2.1. Inner diameter of cylindrical apertures and solid angle for each detector.

Angle (degrees)	Inner diameter (mm)	Solid angle [a)] (str)
11.7	0.5	0.0002
19.5	1	0.0006
27.4	2	0.0026
35.2 - 152.6	4	0.0102
160.4	2	0.0026
168.3	1	0.0006

a) Solid angle for each detector calculated assuming a point scattering source in the center of the PN

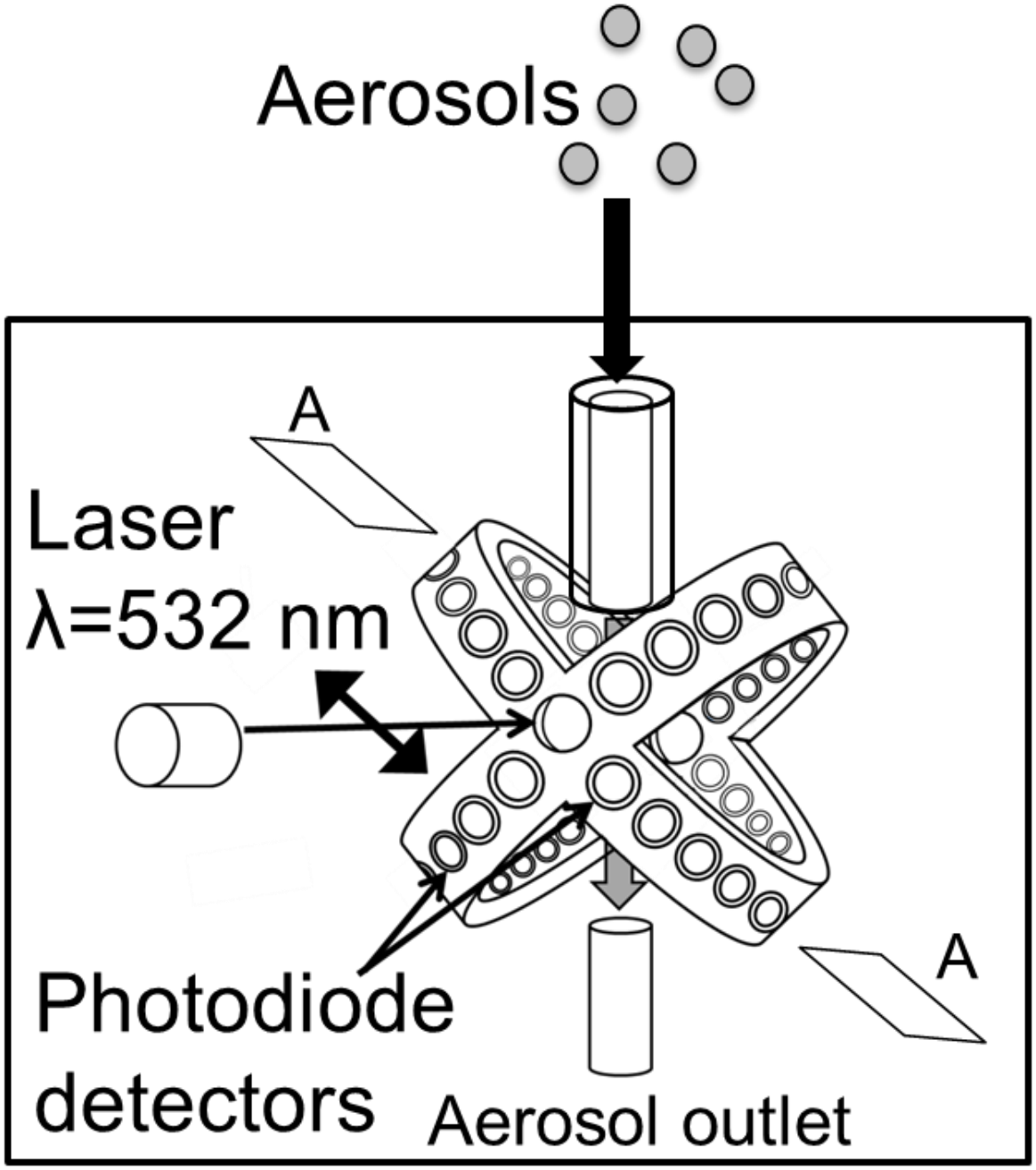

Figure 2.1. Schematic view of the polar nephelometer. The aerosol particles in the sample flow were introduced into the chamber of the polar nephelometer at a flow rate of 0.1 slm surrounded by a sheath flow of 0.3 slm. Scattered incident Nd:YAG laser light from single particles was measured in planes either parallel or perpendicular to the laser polarization. There were 21 photodiode detectors in each plane.

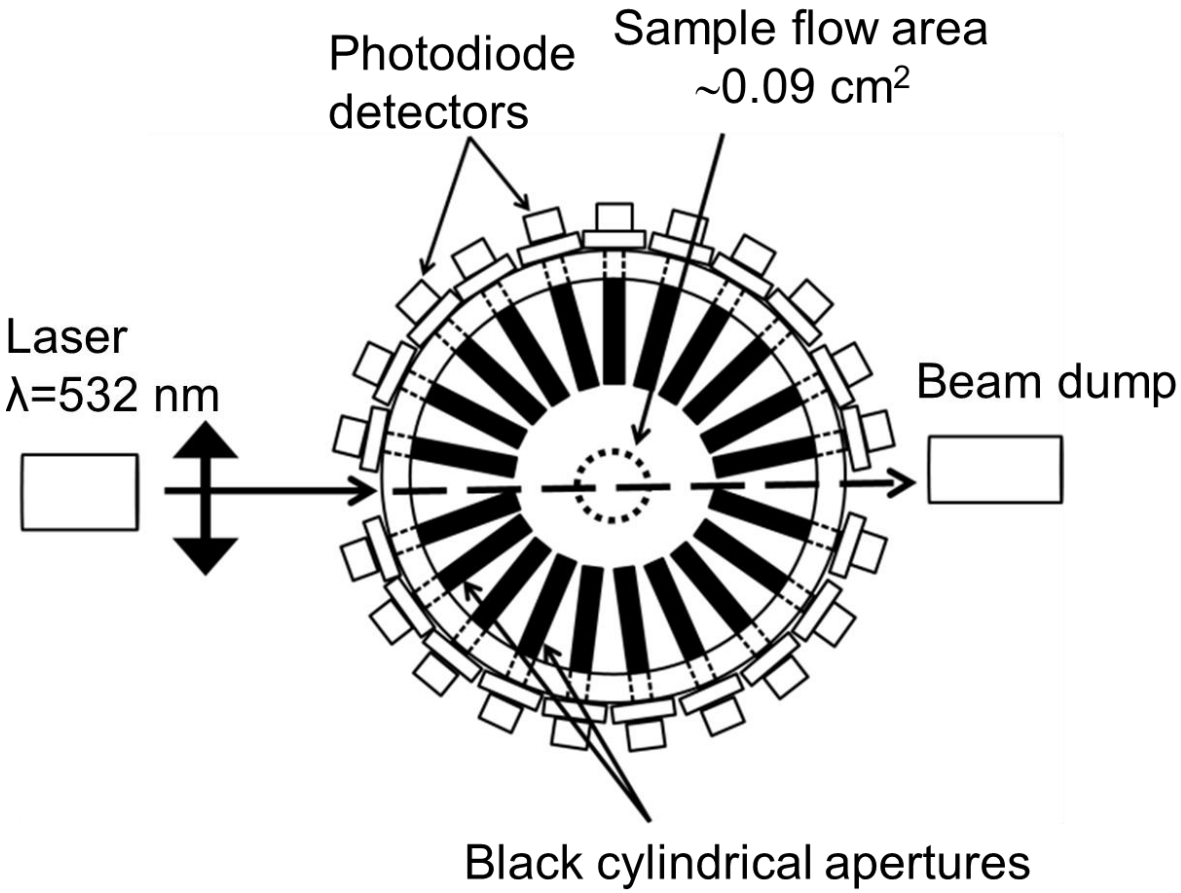

Figure 2.2. Cross-section of the polar nephelometer showing the placement of the photodiode detectors and black cylindrical apertures.

140. 8(L)×73(W) ×46. 2(H) mm^3, 0.6kg

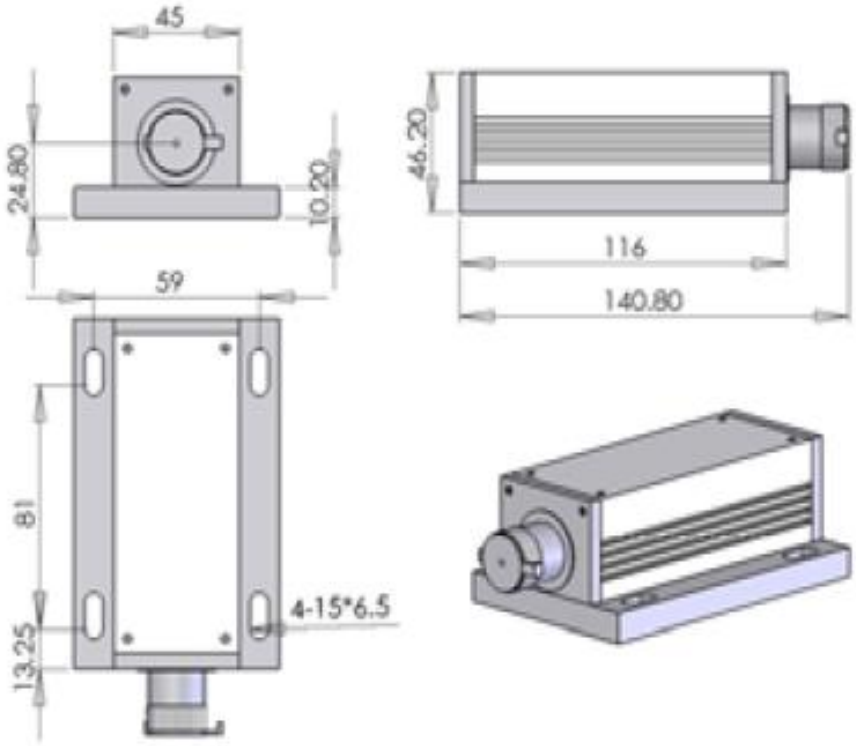

Figure 2.3. Schematic of Nd:YAG laser (Chungchun New Industries, Optoelectronics Technology, Jilin, China, 300 mW).

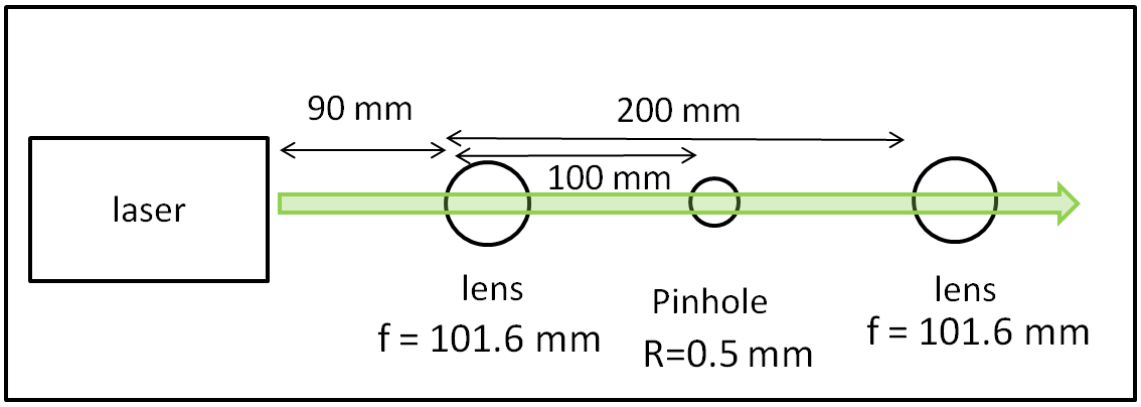

Figure 2.4. This Schematic shows positional relationship between the pinhole, lens and laser.

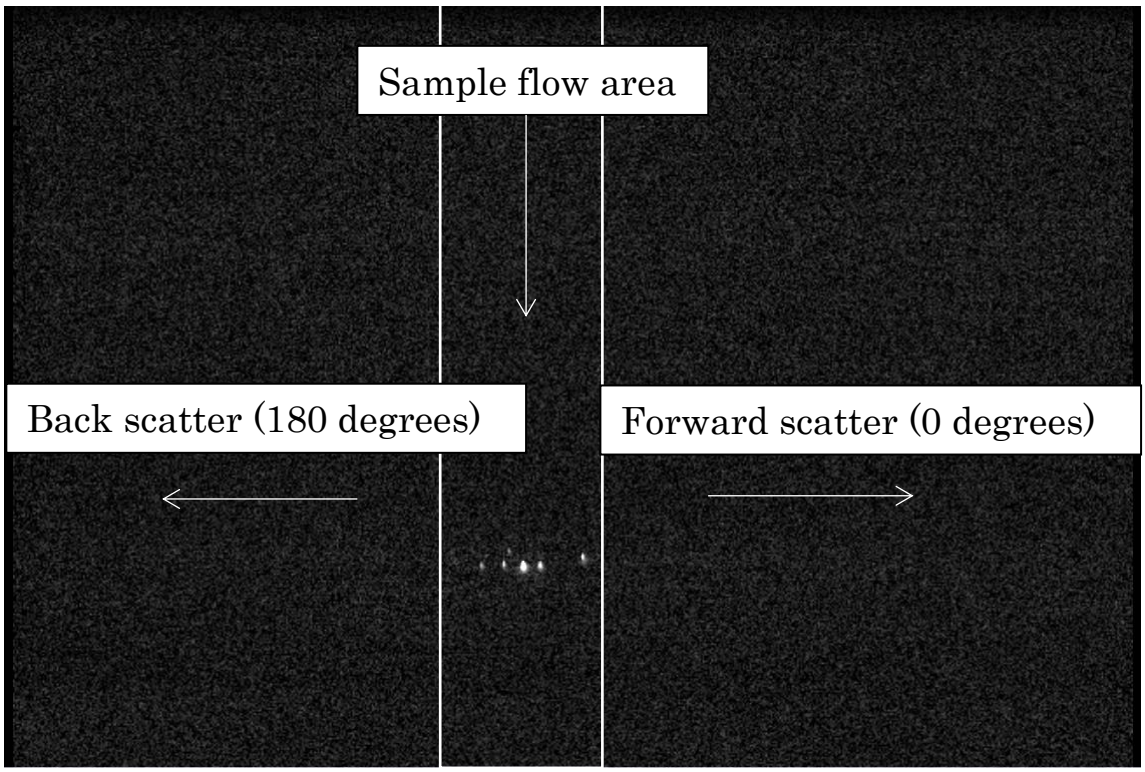

Figure 2.5. CCD image of the scattered light from 707 nm diameter PSL spheres.

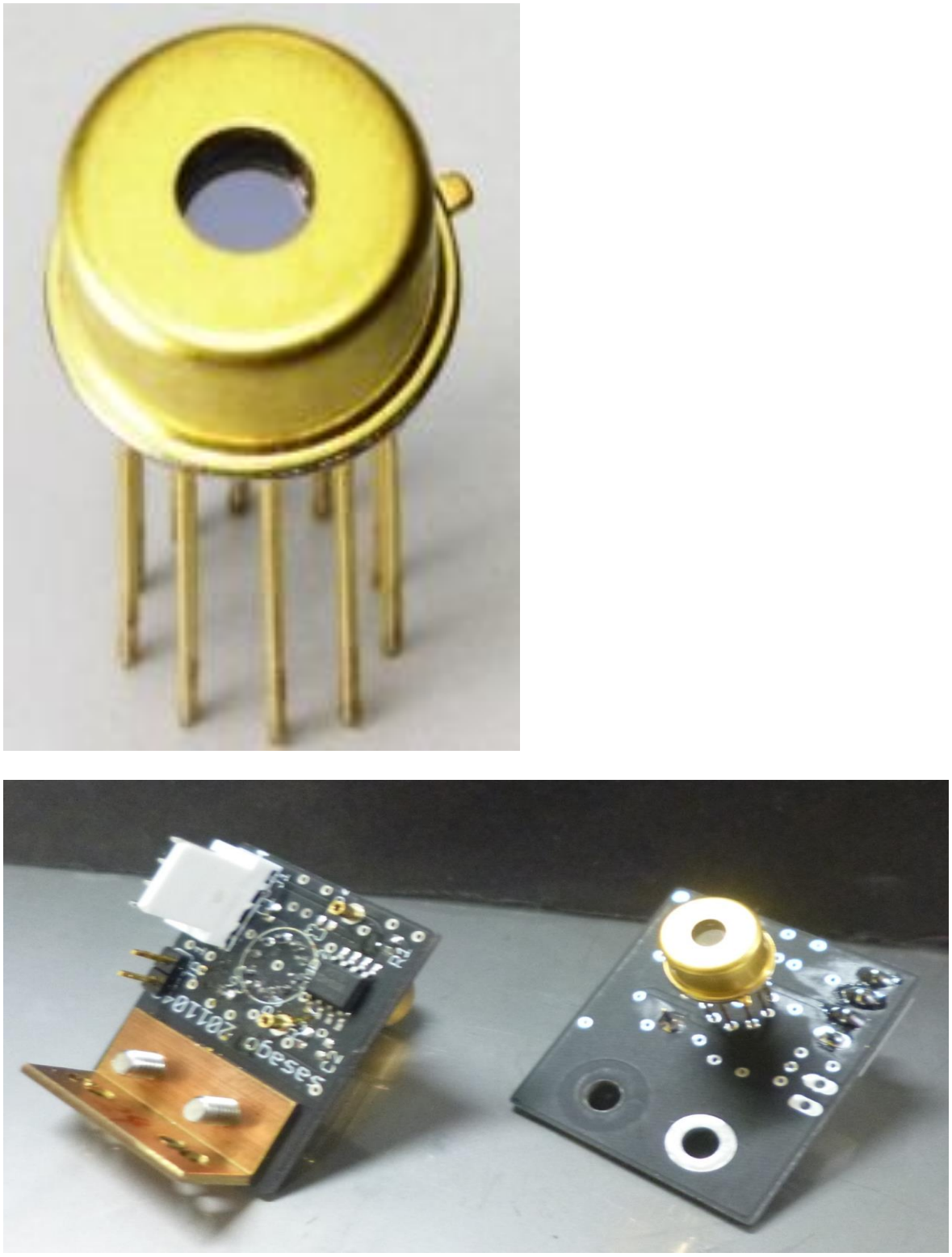

Figure 2.6. Photographs of silicon photodiode detectors (Hamamatsu, S8745-01).

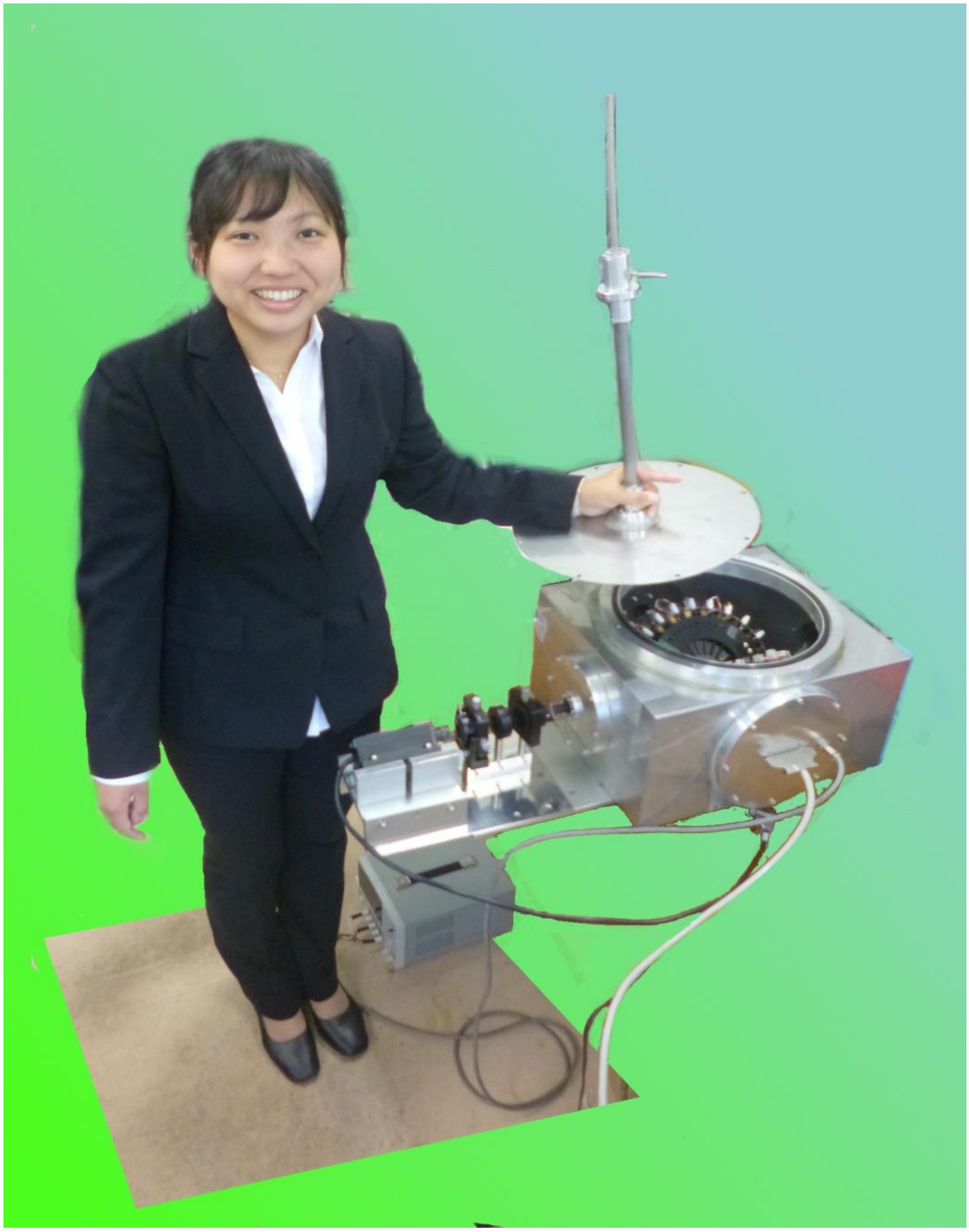

Figure 2.7. Photograph of PN, enclosed in a chamber, 36 cm × 43 cm × 22 cm (33 L).

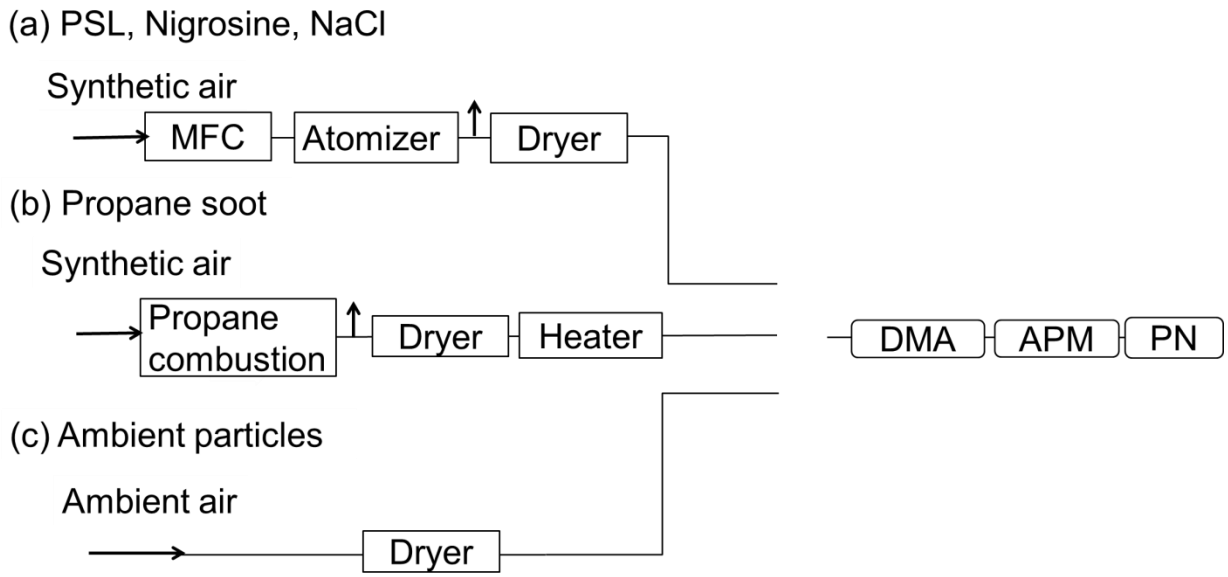

Figure 2.8. Schematic diagrams of the sample handling configurations for (a) mono-disperse polystyrene latex (PSL), sodium chloride (NaCl), and nigrosin particles, (b) propane soot particles, and (c) ambient particles. Legend: DMA: differential mobility analyzer; APM: aerosol particle mass analyzer; PN: polar nephelometer.

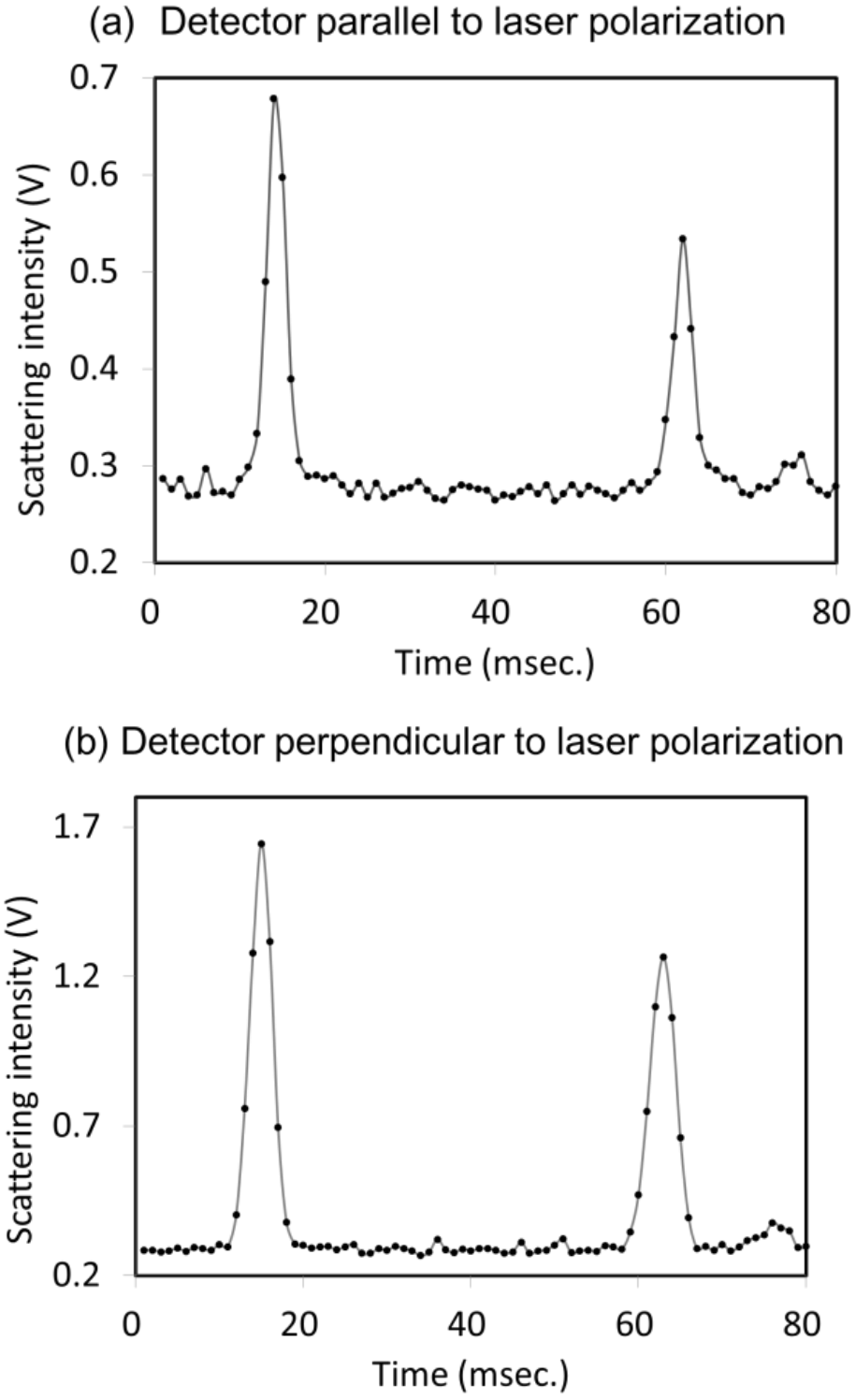

Figure 2.9. Temporal variation of light scattering intensity by two successive PSL particles with mobility diameters of 707 nm for incident light polarized (a) parallel and (b) perpendicular to the scattering plane at 11.7°.

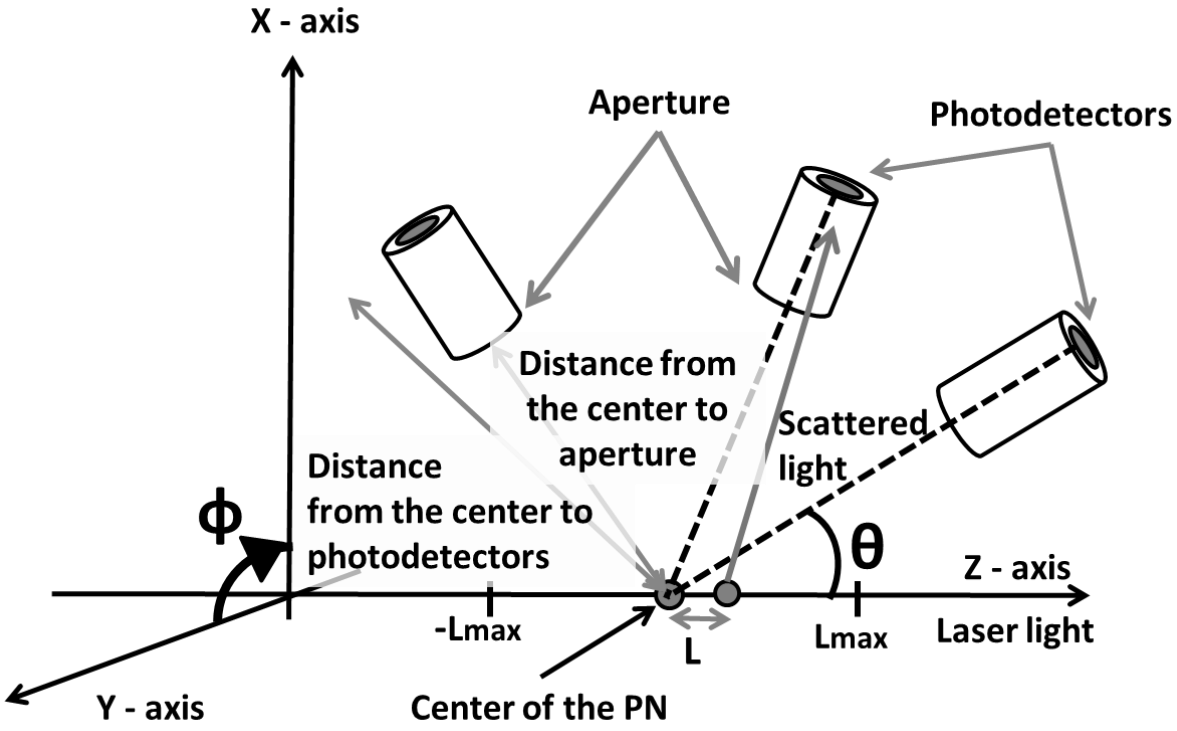

Figure 2.10. Schematic diagram of the optical geometry for the PN. The particles existing along the laser path (0, 0, L ($-L_{max} \leq L \leq L_{max}$)) scatter the laser light. The cylindrical apertures have inner diameters of 4, 2, 1, or 0.5 mm (Table 1). The photoactive diameter of the detectors is 3 mm. Distances from the center to aperture and photodetectors are 35 and 96 mm, respectively. (Proportions in the figure have been adjusted for clarity.)

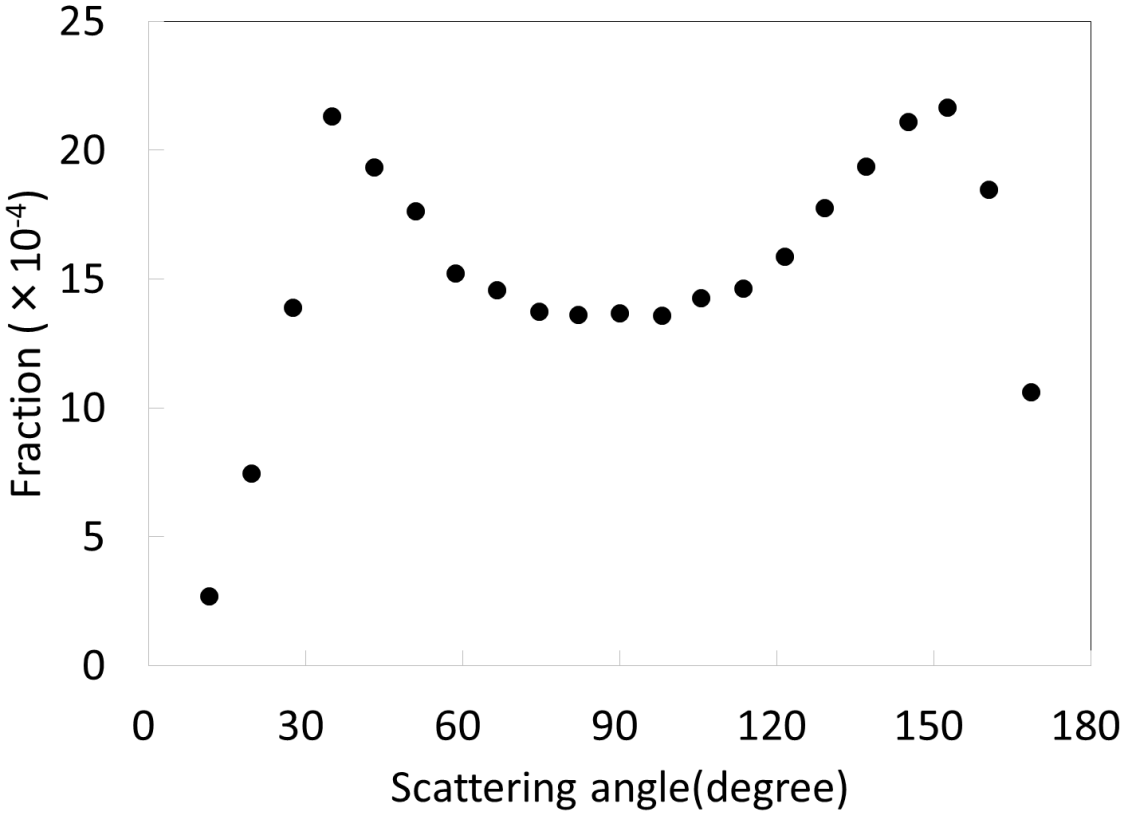

Figure 2.11. Fraction of photons entering each detector calculated using the Monte-Carlo simulation.

Chapter 3

PSL particles

3.1 Introduction

The angular distribution of light scattered by monodisperse polystyrene latex particles (PSL) are measured and compared with Mie theory. The PSL particles are often used for calibration of instrument. Commercially available PSL particle has uniform particle size range from 0.01 to 30 μm, and moderate price (McMurry 2000). Monodisperse PSL particles are relatively easy to generate in the laboratory. The PSL particles with an unequivocal size are atomized with a nebulizer, and then passed through a diffusion dryer, evaporating the solvent. Usually, small surfactant residue particles are also generated during the nebulization of PSL containing solution (Whitby and Liu 1968).Therefore, it is necessary to remove the solid residue particles by DMA and APM. This section focuses on the performance of the new PN to measure the single particles scattering properties of PSL.

3.2 Experimental

The details of the PN used in this study are shown in Chapter2. Only a brief description of the PSL particles experiment will be provided here. PSL particles with diameters of 299 nm, 499 nm, or 707 nm (Thermo Scientific, 3300A, 3500A, and 3700A) were nebulized by an atomizer with filtered, synthetic air (Fig. 2.8a). The PSL particles with mobility diameters of 299, 499, 707 nm were selected using the DMA. The effective densities of PSL particles were assumed to be 1.05 g/cm^3. The DMA and APM were calibrated using the PSL particles, assuming that the certified mean diameters of Thermo Scientific were correct. If the actual diameters of the PSL particles

differed from the certified mean diameters by 2%, it would result in a 6% error in the estimated effective density.

3.3. Results and discussion

To validate the performance of the PN, the angular distributions of scattering for the mono-disperse PSL particles were measured. As shown in Fig. 2.9, there are some variations in the peak intensity for individual particles, likely due to the change in photon density as a function of distance from beam center. Therefore, normalized angular distributions were used for the analyses. Figures 3.1, 3.2 and 3.3 show examples of normalized angular distributions of scattering for three individual PSL particles with mobility diameters of 299, 498, and 707 nm. In total, the angular distributions of 48, 70, and 50 individual PSL particles with mobility diameters of 299, 498, and 707 nm were analyzed and 1σ values for the 48, 70, and 50 individual particles were indicated as error bars in Figs. 3.1, 3.2 and 3.3, respectively. The horizontal axis represents scattering angle, θ, where 0° and 180° correspond to forward and backward scattering, respectively. The scattering distributions of individual particles generally show excellent agreement, although at very weak scattering intensities the low signal-to-noise ratio contributes to greater variation between the measurements at the relevant angles.

The measured angular distributions were compared to the effective angular distributions calculated based on the Lorenz–Mie theory (solid and broken lines in Fig. 3.1, 3.2 and 3.3) after considering the detection efficiency and anglar resolution of each detector, as described in Section 3. In the simulations, the RI of PSL particle at 532 nm was assumed to be $m = 1.60 - 0.00i$ (Nikolov and Ivanov 2000). For all the particle sizes studied, good agreement between the measured and simulated scattering angular

distributions were obtained, as shown in Figs. 3.1, 3.2 and 3.3. Excellent agreement in the magnitude and angle of local minima in scattering were seen in both the simulations and measurements at 137° (Fig. 3.1), 74 and 145 (Fig. 3.2), and 43, 82, 121, and 152.6° (Fig. 3.3). To estimate the influence of the uncertainties in the certified mean diameters of Thermo Scientific, scattering size distributions for the PSL particles with 2% larger and smaller diameters were calculated (Figs. 3.4, 3.5 and 3.6). The observed scattering angular distributions for the PSL particles were still in good agreement with the simulated scattering angular distributions, except for the 2% smaller case in 707 nm PSL particles (Fig. 3.6).

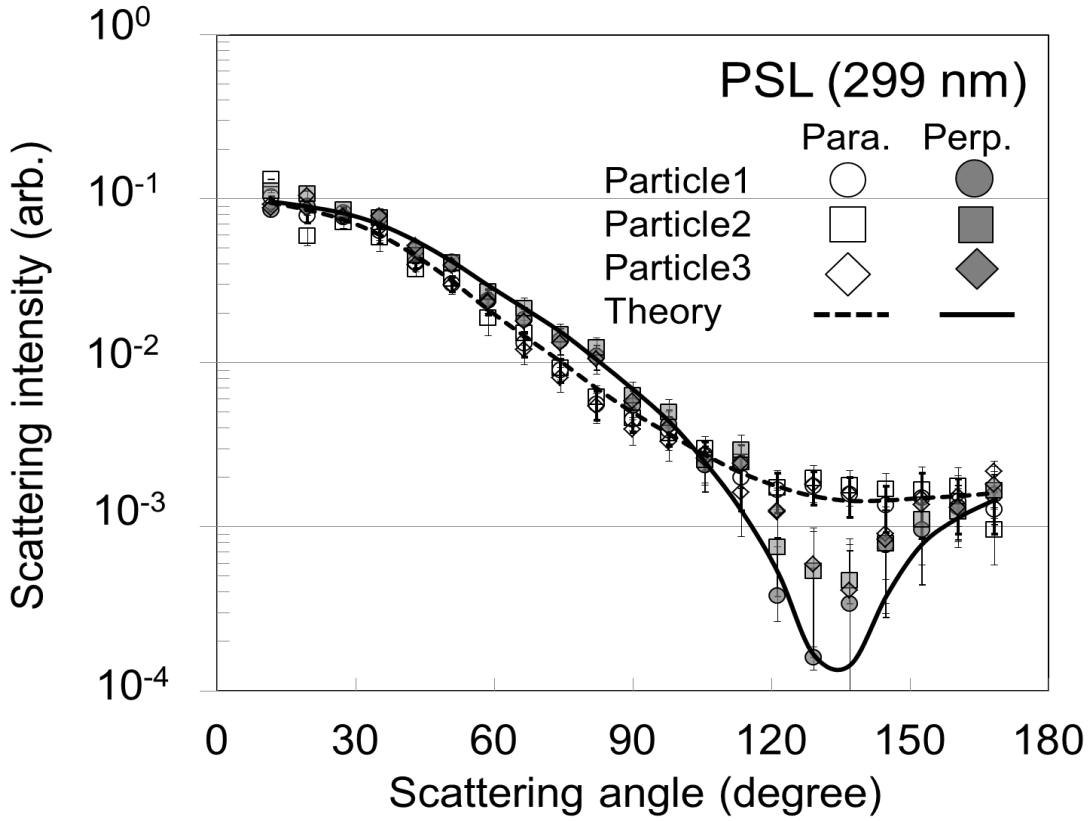

Figure 3.1. Examples of angular distribution of light scattering for incident light polarized parallel (open symbols) and perpendicular (filled symbols) to the scattering plane for three individual PSL particles with mobility diameters of 299 nm. The solid and dashed lines represent the results of simulations based on Lorentz-Mie theory. The open and filled symbols represent the scattering intensities for the laser beam polarized parallel and perpendicular to the scattering planes, respectively. The error bars indicate the 1σ values for 48 individual particles. Note that vertical axis has a log scale.

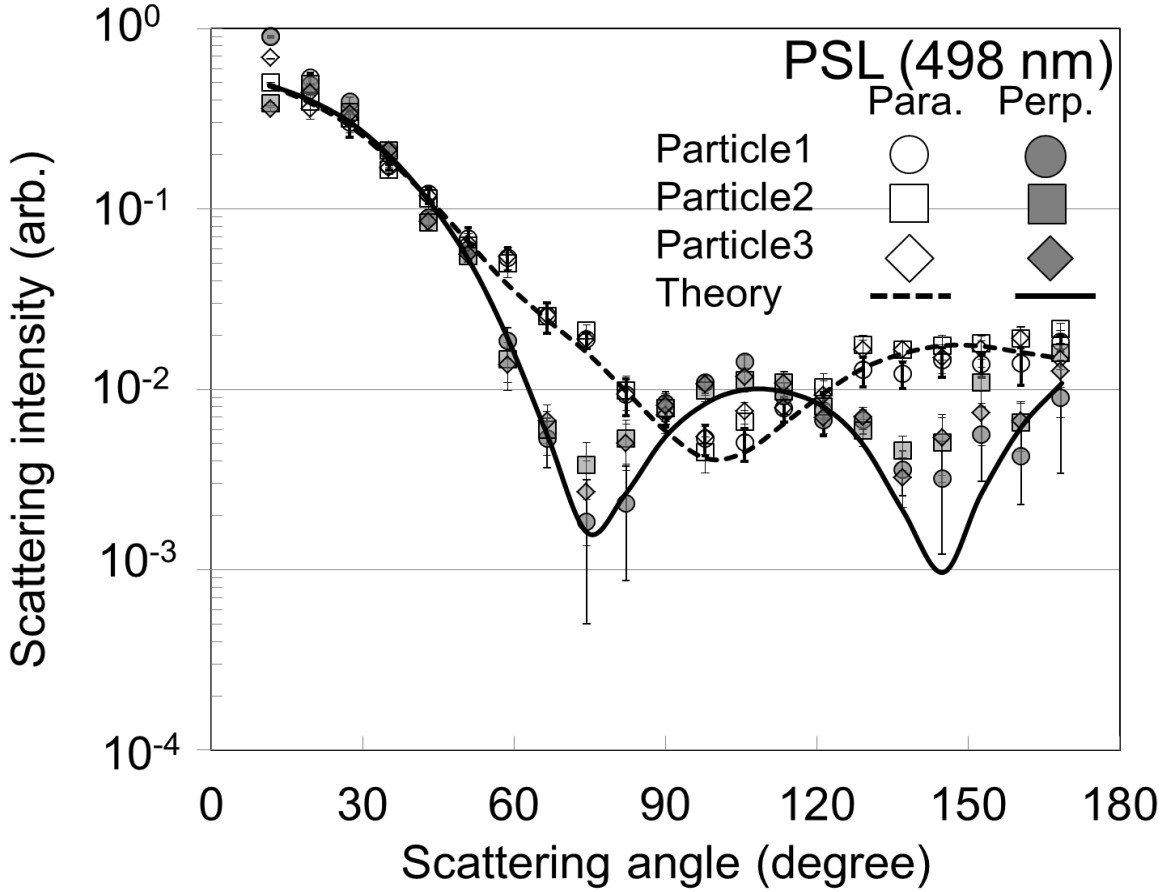

Figure 3.2. The same Fig. 3.1, but PSL particles with mobility diameters of 498 nm and the error bars indicate the 1σ values for 70 individual particles.

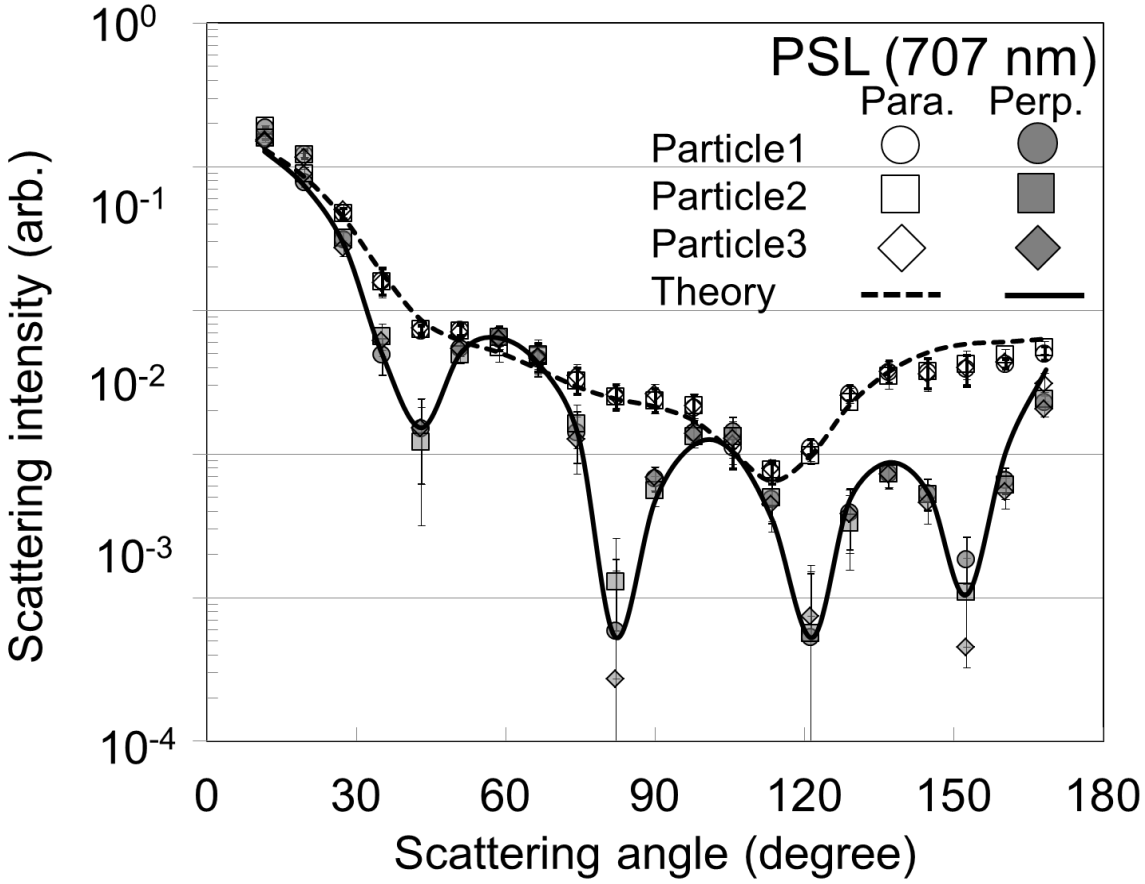

Figure 3.3. The same Fig. 3.1, but PSL particles with mobility diameters of 707 nm and the error bars indicate the 1σ values for 50 individual particles.

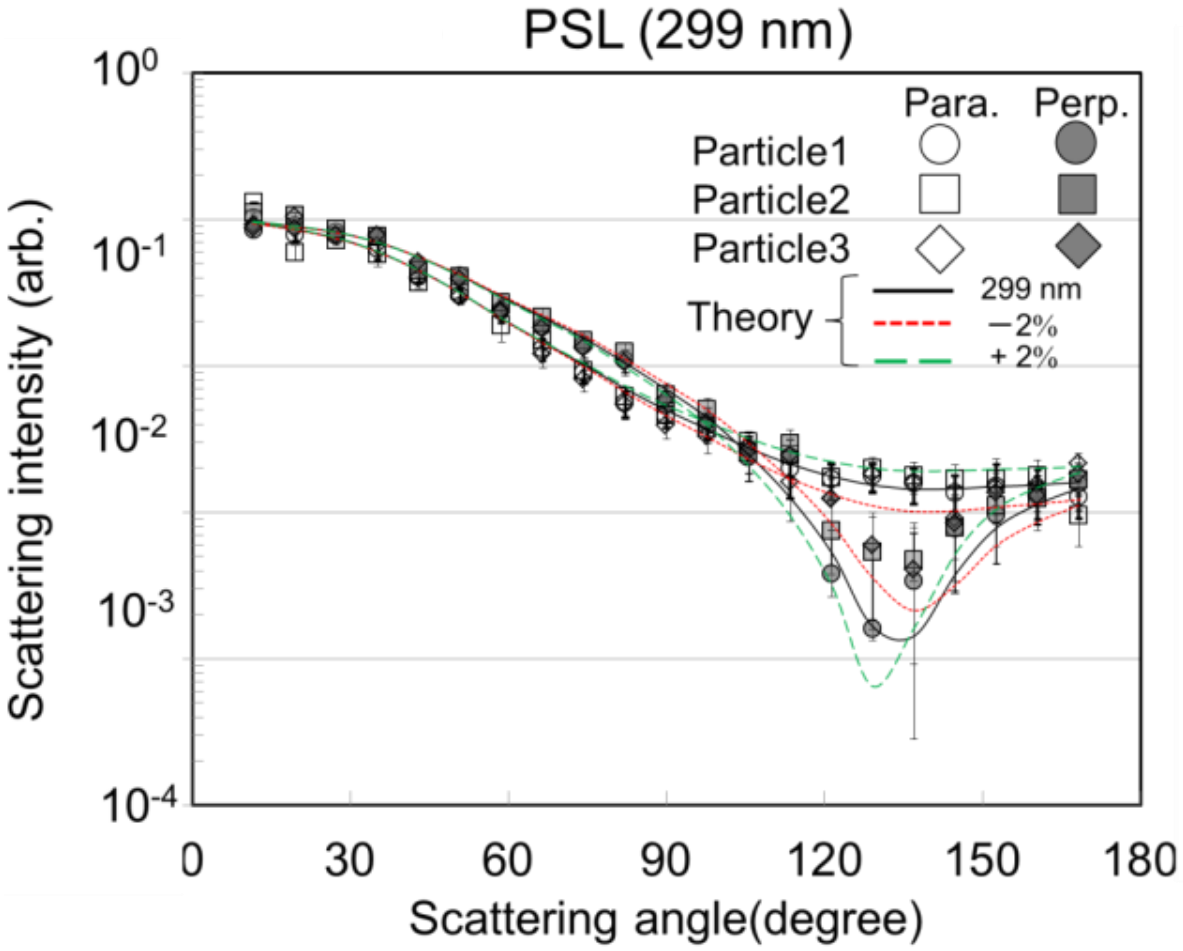

Figure 3.4. Same with Fig. 3.1 but added the theoretical scattering size distributions for the PSL particles with 2% larger and smaller diameters.

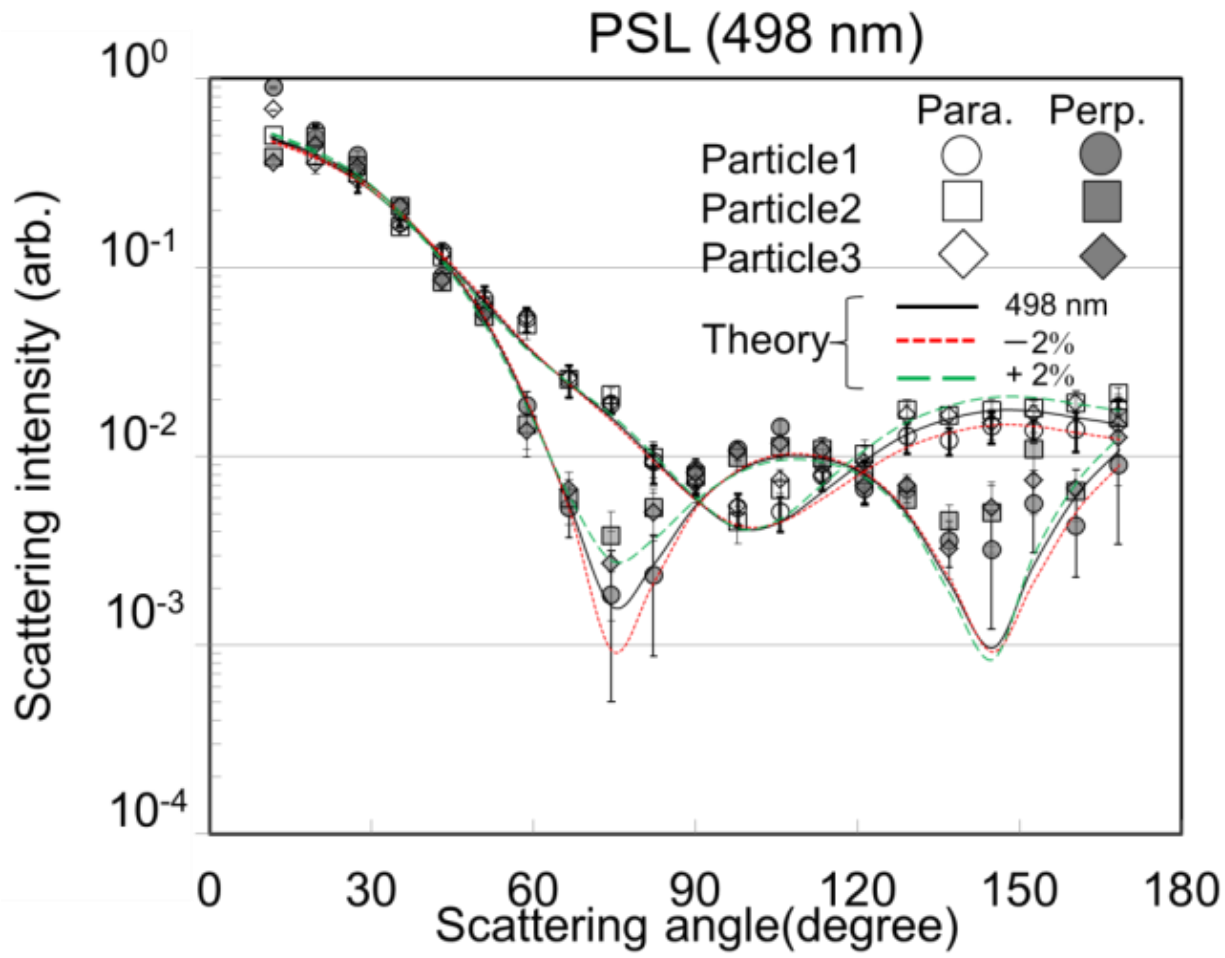

Figure 3.5. The same Fig. 3.4, but PSL particles with mobility diameters of 498 nm.

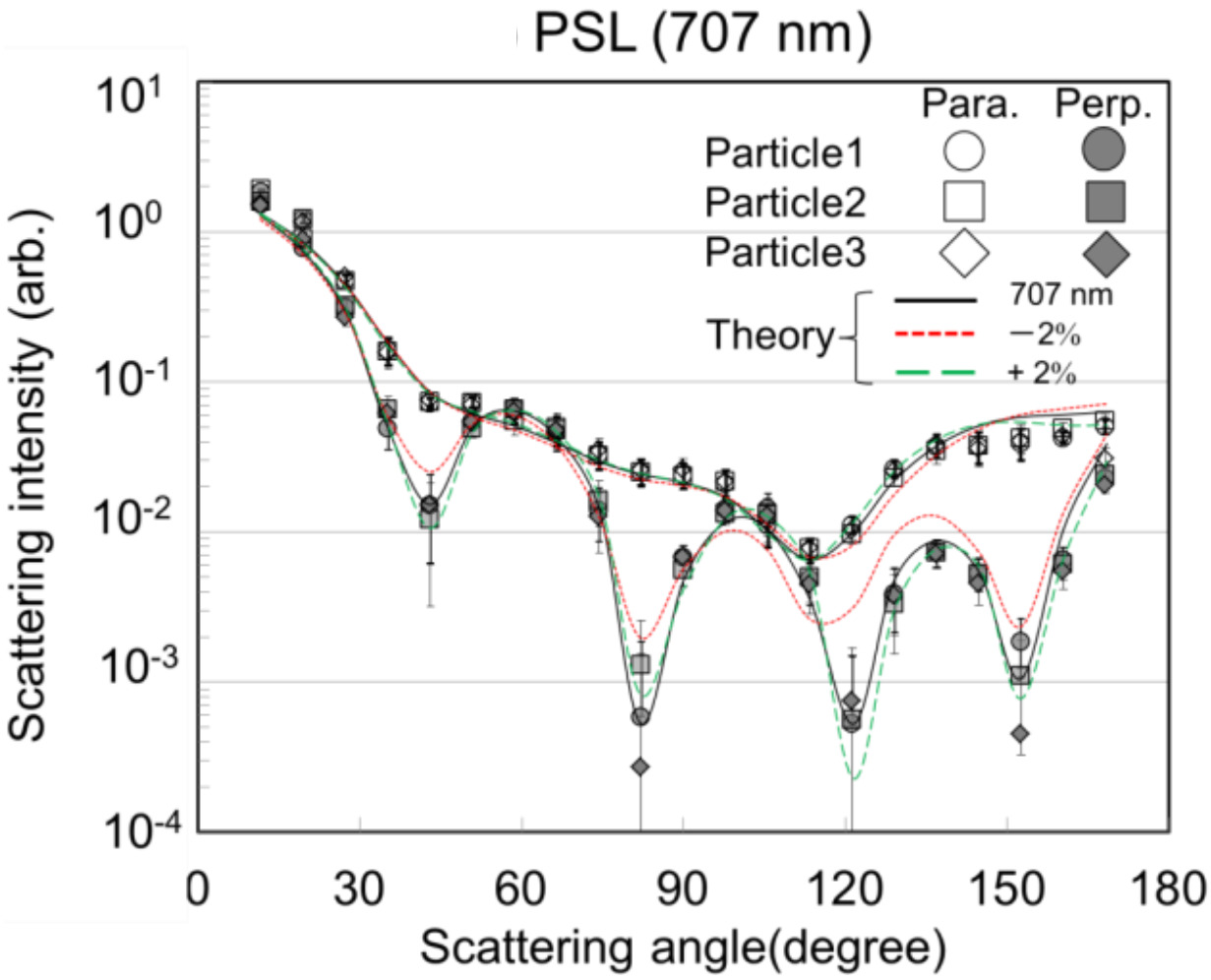

Figure 3.6. The same Fig. 3.4, but PSL particles with mobility diameters of 707 nm.

Chapter 4

Nigrosine particles

4.1 Introduction

Our strategy was to show the angle distribution in light scattering by absorbing particles, and decide the RI for homogeneously nigrosine-dye spheres. The nigrosine is an organic black dye, and dissolved in water and highly absorbing compounds substances. The major industrial applications are as a dyestuff for lacquers and varnishes, in particular, as a black washable marker-pen for schools (Schmitt 1944). It is soluble not only in water but also in oils. Nigrosine particles are also used for the calibration of instrument to measure light absorption of particles (Hoffer et al. 2016).

In general, the RI is represented by the real part *n*, and imaginary part *ik*.

$$m = n - ik$$

where *n* and *ik* associated to the light scattering and the light absorbing, respectively. Several approaches for measuring RI have been reported. Flores et al. (2012) determined RI value for dry nigrosine particle to be m = 1.626 (± 0.021) - 0.243 (± 0.023)i at 532 nm, using cavity ring-down spectroscopy. Woo et al. (2013) also reported the RI of nigrosine to be 1.70 - 0.24i at 670 nm by measuring absorption coefficients using a multiangle absorption photometer. Liu et al. (2013) also used nigrosine for the calibration of ellipsometer and reported RI value of nigrosine to be m=1.61 (± 0.01) - 0.23 (± 0.01)i at 532 nm.

4.2 Experiment

The details of the PN used in this study are shown in Chapter2. Only a brief

description of the nigrosine particles experiment will be provided here. Aqueous solutions of nigrosine dye (Aldrich) were nebulized by an atomizer with filtered, synthetic air (Fig. 2.8a).

The nigrosine particles with mobility diameters of 300, 500, and 700 nm were selected using the DMA and APM. The effective densities of nigrosine particles were assumed to be 1.59 g/cm^3. The Aqueous solutions of nigrosine dye were generated with the handling used for the PSL particles. We determine the RI by analyzing the measured angular distributions of scattering data.

4.3. Results and discussion

Figures 4.1, 4.2 and 4.3 show averages of the normalized angular distributions of scattering for 45, 69, and 69 individual nigrosine particles with mobility diameters of 300, 500 and 700 nm, respectively. Nigrosine absorbs strongly at visible wavelengths. Several previous studies have estimated the RI of nigrosine particles: Reported *n* values near 532 nm ranged from 1.61 to 1.72, while *k* values ranged from 0.23 to 0.31.(Garvey and Pinnick 1983; Lack et al. 2006; Dinar et al. 2008; Lang-Yona et al. 2009; Flores et al. 2012; Liu et al. 2013). Our measured angular distributions were compared to the results of the Monte-Carlo simulation and the RI values were optimized to minimize the sum of the squared residual between the logarithms of observed and simulated scattering intensities. The *n* value was fixed between 1.3 and 1.8 and the *k* value was fixed between 0.00 and 0.50. The results of the Monte-Carlo simulation with the optimized RI values were shown with solid and dashed lines in Figs. 4.1, 4.2 and 4.3. The optimized RI values were determined to be $m = (1.60 \pm 0.01) - (0.14 \pm 0.09)i$, $m = (1.61 \pm 0.01) - (0.14 \pm 0.04)i$, and $m = (1.60 \pm 0.01) - (0.11 \pm 0.11)i$ for nigrosine

particles with mobility diameters of 300, 500, and 700 nm, respectively, where quoted uncertainties represent 1σ values for 45, 69, and 69 individual particles. The obtained *n* and *k* values were consistent among the three diameters. These results suggest that *n* and *k* values for individual particles can be determined with typical statistical uncertainties of 0.01 and 0.04-0.11, respectively. Our *n* values are close to the reported value by Liu et al. (2013) (*n* = 1.61 at 530 nm), while our *k* values are somewhat lower than those of earlier studies. Although the reason for the lower *k* values is unclear, the PN should be less sensitive to *k* value considering the larger statistical uncertainties for the *k* value compared to the *n* value.

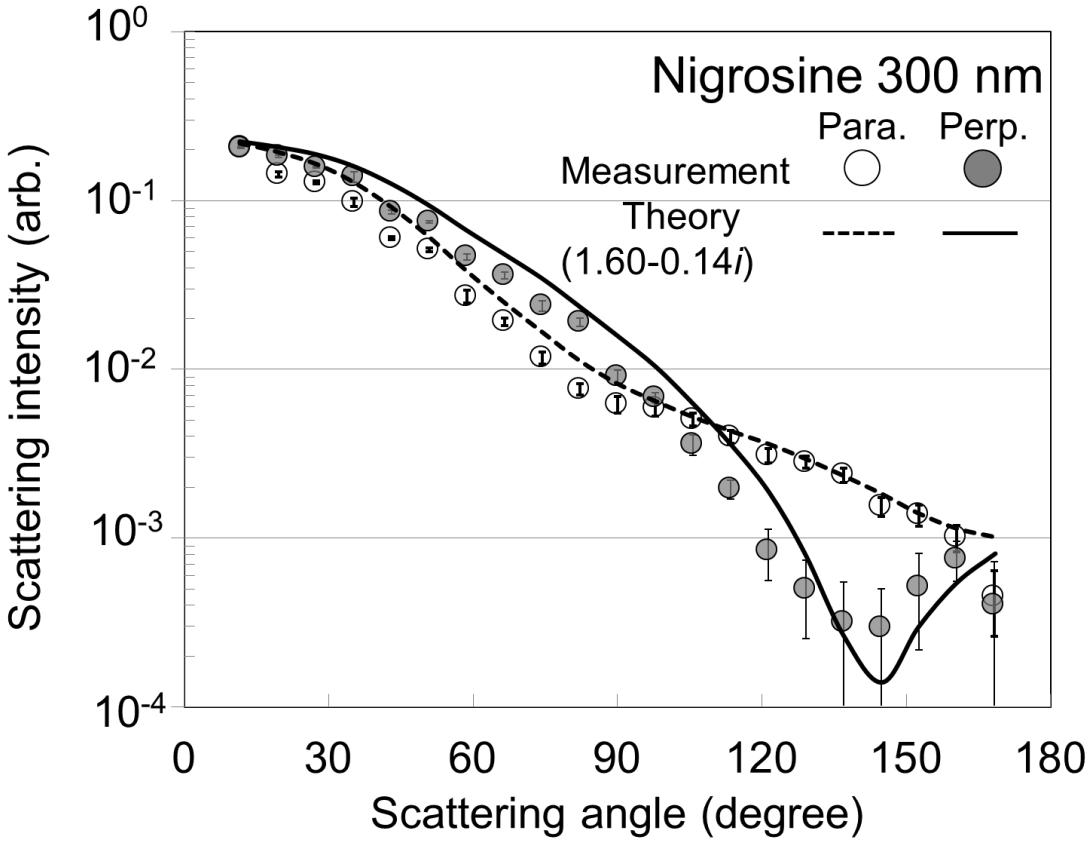

Figure 4.1. Averaged angular distribution of light scattering for incident light polarized parallel (open symbols) and perpendicular (filled symbols) to the scattering plane for individual nigrosine particles with mobility diameters of 300 nm. The error bars indicate the 1σ values for 45 individual particles. The solid and dashed lines represent the results of simulations based on Lorentz-Mie theory with optimized RI values. Note that the vertical axis has a log scale.

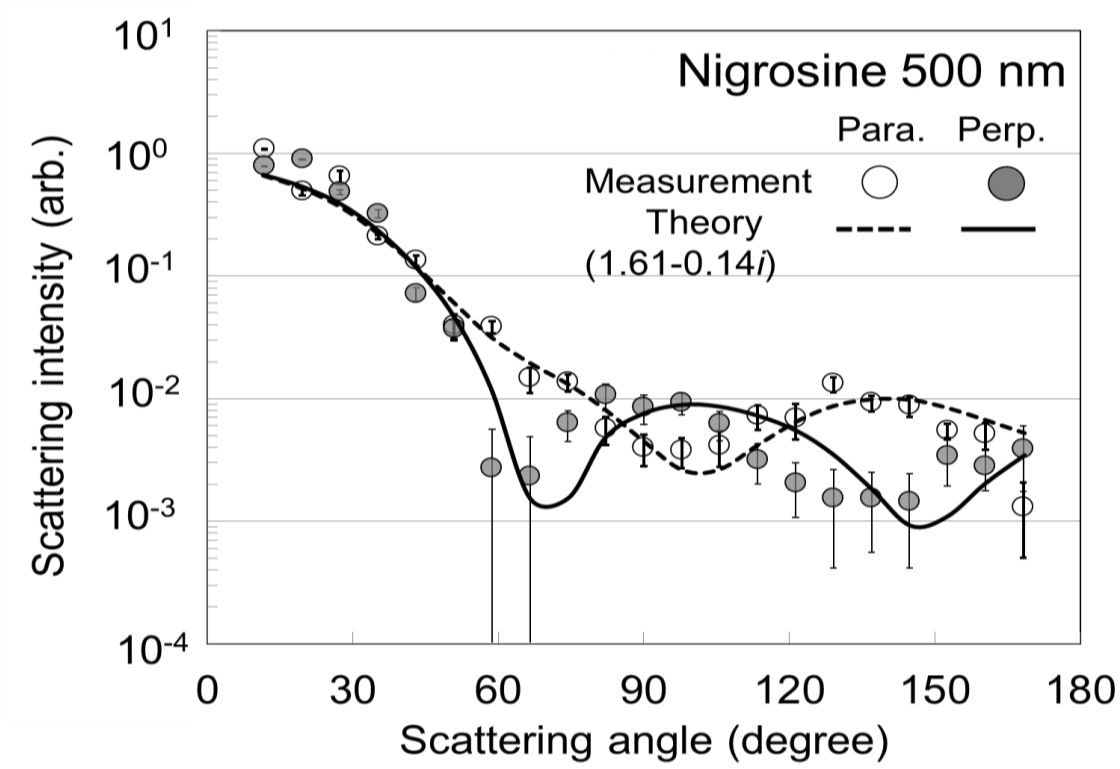

Figure 4.2. The same with Fig. 4.1, but nigrosine particles with mobility diameters of 500 nm and the error bars indicate the 1σ values for 69 individual particles.

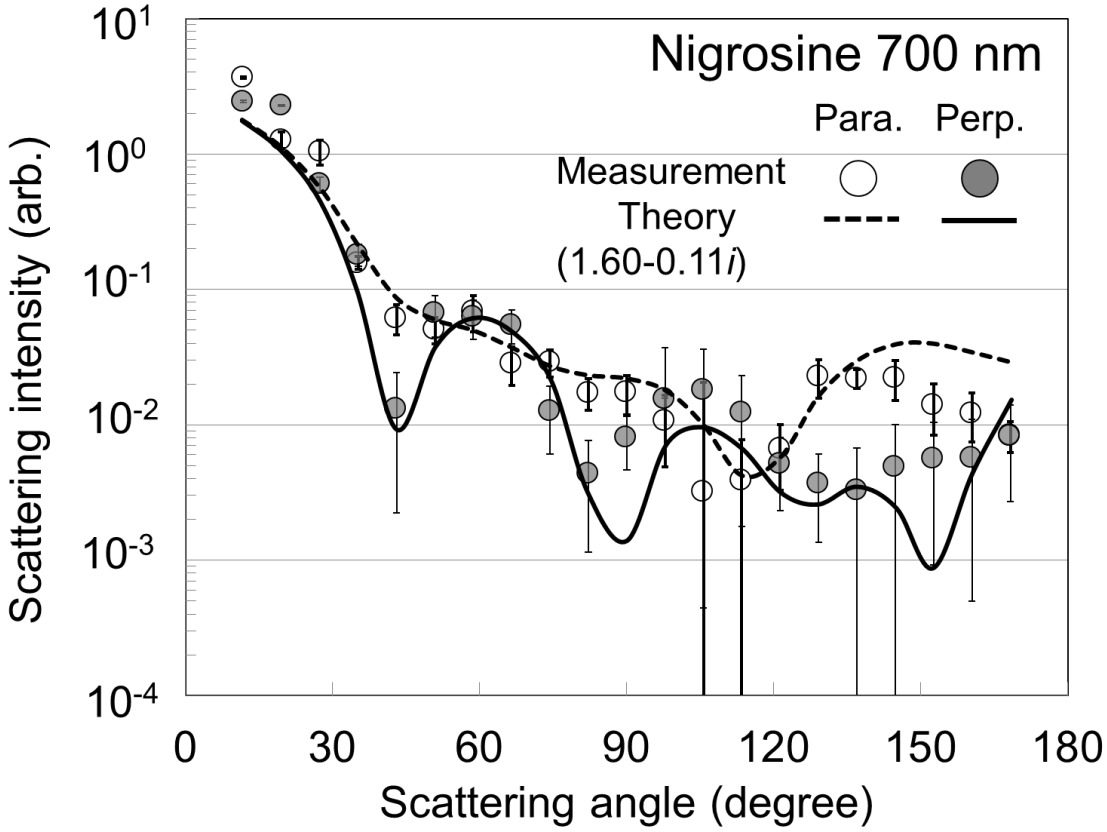

Figure 4.3. The same with Fig. 4.1, but nigrosine particles with mobility diameters of 700 nm and the error bars indicate the 1σ values for 69 individual particles.

Chapter 5

NaCl particles

5.1 Introduction

This Chapter focuses on sodium chloride particles (NaCl). Considering that non-spherical particles exist ubiquitously in the atmosphere, understanding of optical properties of non-spherical particles is important. It is known that the angular distributions of scattering of non-spherical particles depended strongly on shape parameters. The NaCl particles are a kind of hygroscopic inorganic salt particles. The shape of these particles can be varied depending on their generation, drying, and aging processes. The NaCl particles typically have cubic in shape with rounded edges and corners. Previous studies reported the light scattering properties of randomly oriented NaCl particles (Pinnick et al. 1976; Perry et al. 1978). The real part of RI was reported to be $m = 1.55 - 0.00i$ at 532 nm. (Pinnick and Auvermann, 1979).

Here we investigate angular distributions of scattering for individual NaCl particles with mobility diameters of 300, 500, and 700 nm, and make a comparison of the scattering measurement with Mie theory curves.

5.2. Experiment

The details of the PN used in this study are shown in Chapter2. Only a brief description of the NaCl particles experiment will be provided here. Aqueous solutions of sodium chloride (NaCl, Wako Chemicals) were nebulized by an atomizer with filtered, synthetic air (Fig. 2.8a). The NaCl particles with mobility diameters of 300, 500, and 700 nm were selected using the DMA. The rotation velocity and voltage of the

APM for NaCl were chosen based on effective density distribution measurements from the DMA, the APM, and a condensation particle counter (CPC) (TSI, model 3772). Average effective densities for NaCl particles with mobility diameters of 300, 500, and 700 nm, were estimated to be 1.87, 1.84, and 1.81 g/cm^3, respectively. Size selected NaCl particles were also collected on carbon-coated nitrocellulose (collodion) films using a cascade impactor (50% cutoff aerodynamic diameter of a stage was 0.26 μm at a flow rate of 0.4 L min^{-1}) for morphological analysis by a transmittance electron microscope (TEM) (JEOL, JEM-2010).

5.3. Results and discussion

The NaCl particles generated in the present study under dry conditions were cubic in shape with rounded edges and corners, as shown in TEM images (Fig. 5.1). Figure 5.2 shows averages of normalized angular distributions of scattering for individual NaCl particles with mobility diameters of 300, 500, and 700 nm, along with the simulated angular distributions (assuming spherical NaCl particles). In the simulations, the RI of NaCl particles at 532 nm was assumed to be m = 1.55 - 0.00i (Pinnick and Auvermann, 1979). Theoretical distributions based on the Lorenz–Mie theory for spherical particles with volume equivalent diameters (estimated from the effective densities measured using the combination of the DMA, APM, and CPC) were also plotted in Figs. 5.2, 5.3 and 5.4.

Differences in the measured and simulated scattering angular distributions were observed for particles with mobility diameters of 500 and 700 nm, as shown in Figs. 5.2, 5.3 and 5.4. The simulations predicted local minimum values at ~75° and ~145° (500 nm, Fig. 5.3), and at ~60°, 80°, 105° 115°, and 150° (700 nm, Fig. 5.4) for

perpendicular polarization. These minima were not evident in the PN measurements. For smaller NaCl particles with a mobility diameter of 300 nm, relatively good agreement between measured and simulated scattering angular distributions was observed. These results are qualitatively consistent with previous reports (Pinnick et al. 1976; Perry et al. 1978) and can be explained theoretically based on the particle size dependence of interference of scattered light (Bohren and Clothiaux 2006). When particles are sufficiently small compared to the wavelength of incident light, waves scattered by the different dipoles are approximately in phase for all scattering directions and the scattering angular distribution is not strongly dependent on particle shape. In contrast, with larger particles the phase shift between dipoles becomes significant and therefore several local minima are expected to appear in the scattering angular distribution when a spherical particle shape is assumed. Because larger variations in the degree of phase difference are expected for irregularly shaped particles compared to spherical particles, the amplitude of the oscillation in the scattering angular distribution for realistic cuboid NaCl particles should be less than that for spherical particles. In this study, good agreements between measured and simulated scattering angular distributions were observed at smaller scattering angles (<40°) for all particle sizes. The results are also consistent with the theoretical prediction that the waves scattered by the different dipoles in the forward direction are approximately in-phase regardless of the particle size (Bohren and Clothiaux 2006). These results suggest that our PN has the potential to distinguish between spherical and non-spherical particles, especially when particle diameters exceed ~500 nm.

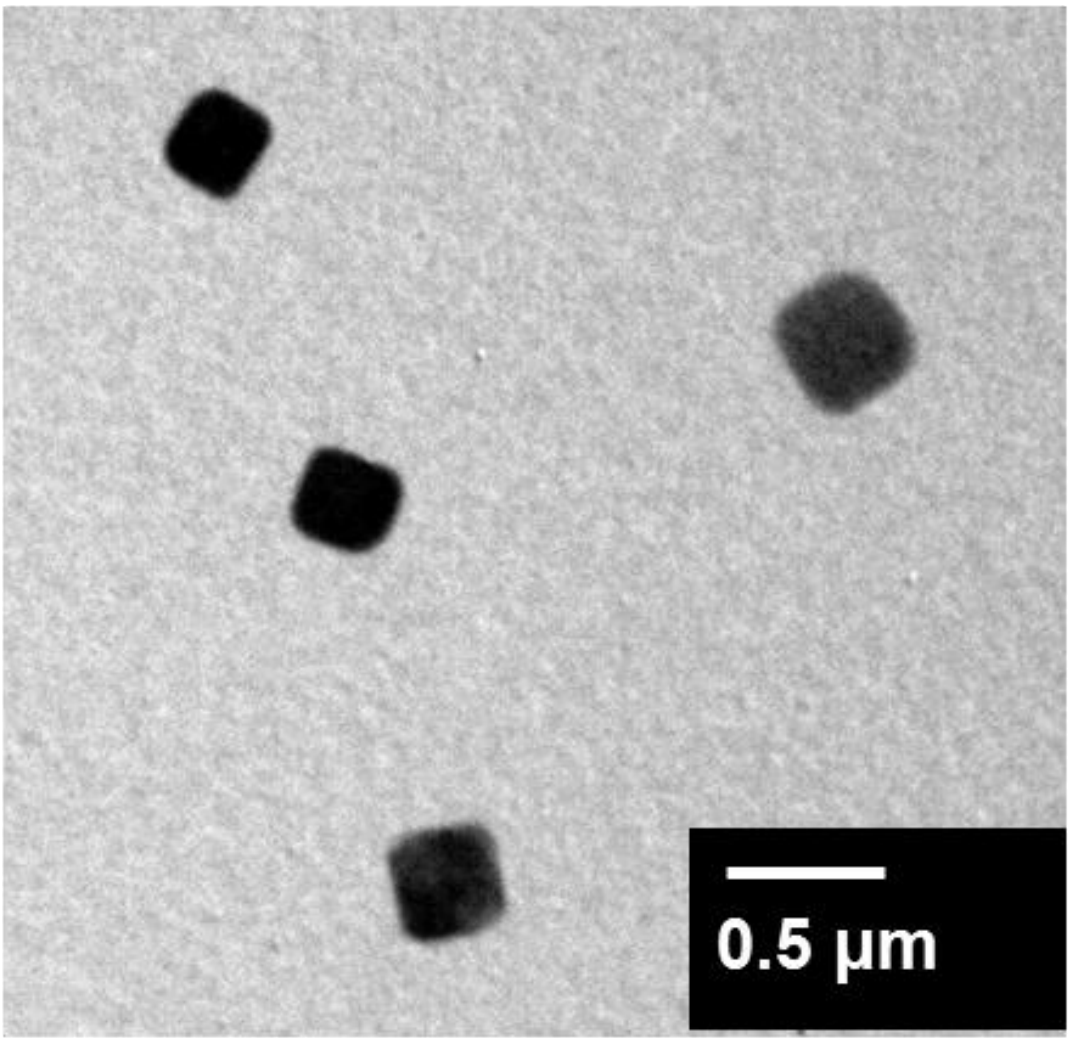

Figure 5.1. TEM images for NaCl particles with mobility diameter of 300 nm.

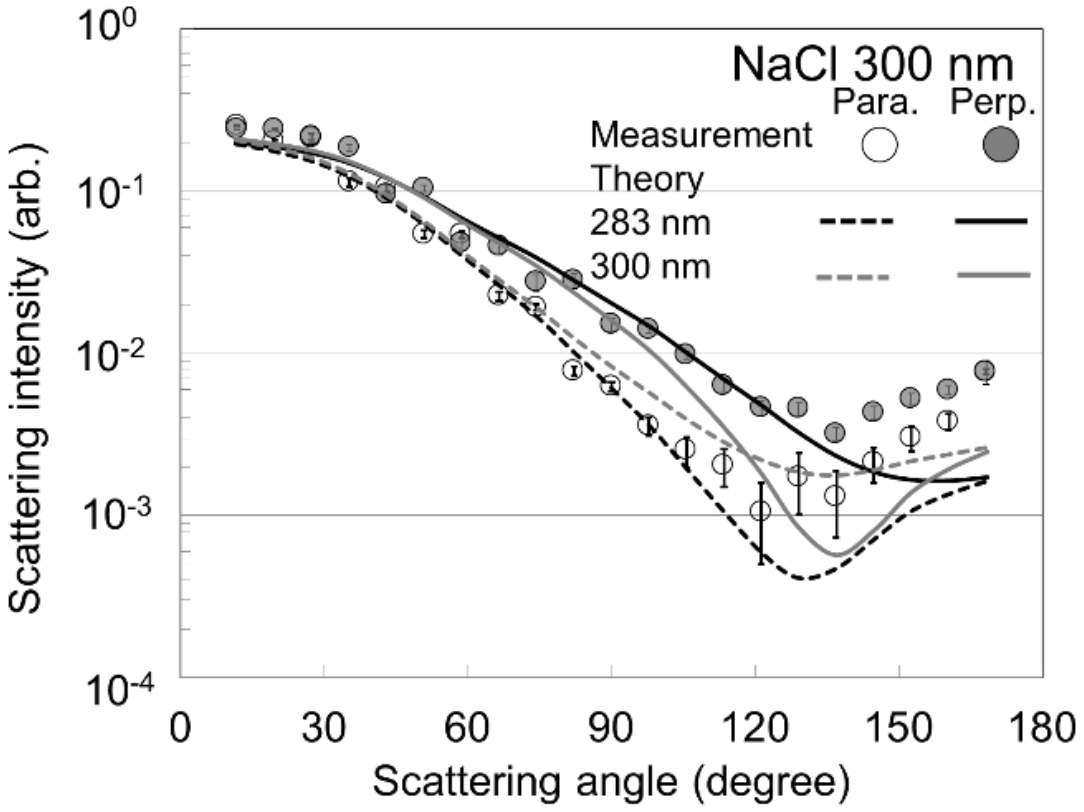

Figure 5.2. Averaged angular distribution of light scattering for incident light polarized parallel (open symbols) and perpendicular (filled symbols) to the scattering plane for individual NaCl particles with mobility diameters of 300 nm. The error bars indicate the 1σ values for 60 individual particles. The solid and dashed lines represent the results of simulations based on Lorentz-Mie theory and assuming spherical particles. Note that the vertical axis has a log scale.

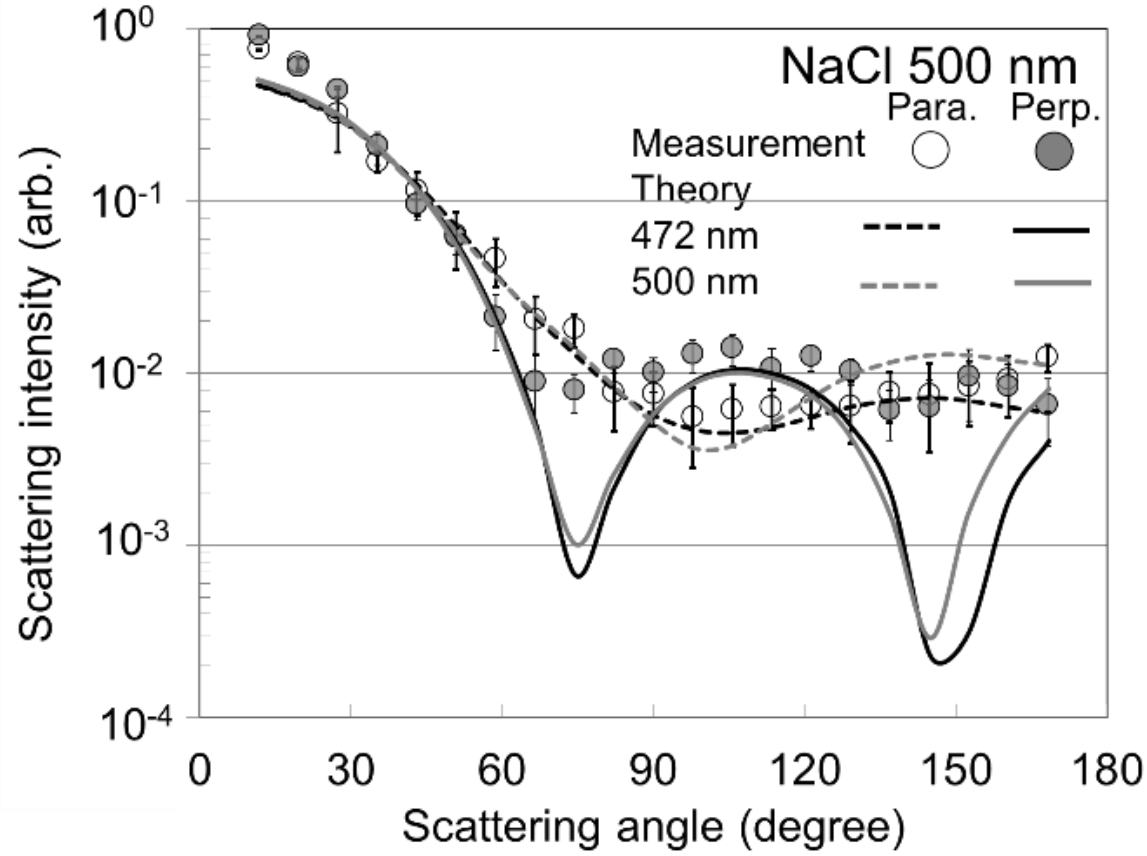

Figure 5.3. The same with Fig. 5.2, but NaCl particles with mobility diameters of 500 nm.

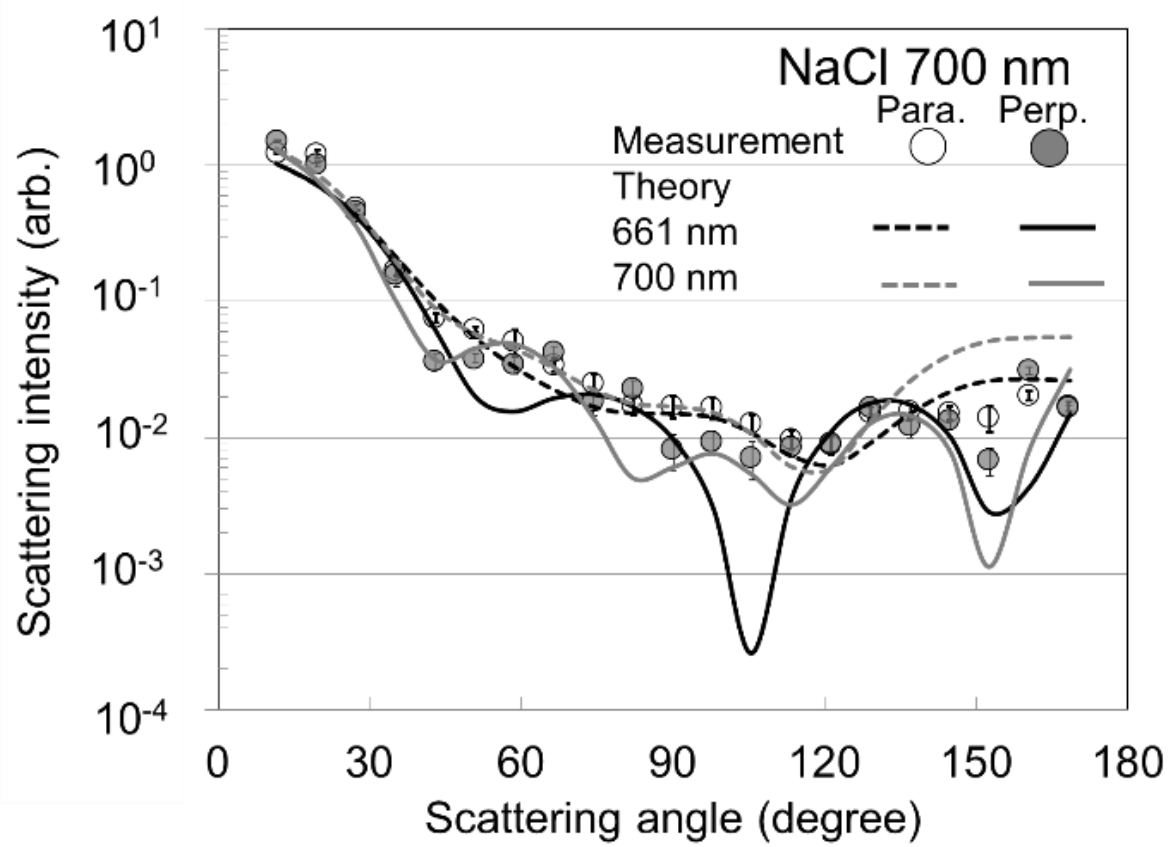

Figure 5.4. The same with Fig. 5.2, but NaCl particles with mobility diameters of 700 nm.

Chapter 6

Soot particles

6.1 Introduction

Black carbon (BC) and soot particles are combustion-generated particles, mostly released from combustion of diesel fuel, gasoline, biomass, petroleum oil and coals (Adachi et al.2011, Chen et al. 2005, Kim et al. 2015). This Chapter focuses on soot, which has one of the most important roles in the Earth's atmosphere and their optical properties affect direct and indirect radiative forcing. The soot particles have irregular and random structure (Farias et al. 1996, Köylü and Faeth 1994). The absorption and scattering properties of soot particles depend on their morphologies (Kim et al. 2015). The soot particles are consisted of monomer spherical particles with diameters between 10 and 100 nm, and created grape-like branched clusters. Freshly emitted soot particles often composed of a lacey morphology. This morphology might be changed to compact configuration after water uptake and removal (Radney et al. 2014). We use freshly emitted soot particles in this study.

The morphology of soot is described by relationship between the number of monomers in an agglomerate, N, and the radius of gyration of the agglomerate, R_g. These morphology of soot obey the following relationship

$$N = k_0 \left(\frac{R_g}{D_{mon}} \right)^{D_f}$$

where D_{mon} is the diameter of a monomer, k_0 is the fractal prefactor, and D_f is the fractal dimension. The RI and D_f values of fresh soot are close to1.95–0.79i at 550 nm, and 1.8, respectively (Bond and Bergstrom 2006). Here we investigate angular

distributions of scattering for individual soot particles with mobility diameters of 300, 500, and 700 nm, and make a comparison of the scattering measurement with Mie theory curves.

6.2. Experiment

The details of the PN used in this study are shown in Chapter2. Only a brief description of the soot particles experiment will be provided here. A burner operating on propane fuel was used to generate soot particles (Fig. 2.8b). Because these soot particles may be internally mixed with organic materials, the particles were first dried and then passed through a heater maintained at 300°C to remove organic materials. The design and performance of the heater was provided in other publications (Guo et al. 2014; Nakayama et al. 2014).

Propane soot particles with mobility diameters of 300, 500, and 700 nm were selected using the DMA. The APM was not used for size selection of soot particles during the scattering angular distribution measurements. In a separate experiment, average effective densities of propane soot particles with mobility diameters of 300, 500, and 700 nm were determined using the DMA-APM-CPC system to be 0.20, 0.12, and 0.09 g/cm^3, respectively. The observed trend of decreasing effective density with increasing mobility diameter is consistent with previous studies on the effective densities of soot particles (*e.g.*, Park et al. 2003, Xue et al. 2009).

Size selected propane soot particles were also collected on carbon-coated nitrocellulose (collodion) films using a cascade impactor (50% cutoff aerodynamic diameter of a stage was 0.26 μm at a flow rate of 0.4 L min^{-1}) for morphological analysis by a transmittance electron microscope (TEM) (JEOL, JEM-2010).

6.3. Results and discussion

The propane soot particles generated in the present study had aggregate structures characteristic of soot comprising small spherules with a typical diameter less than <100 nm (Fig. 6.1). Figures 6.2, 6.3 and 6.4. show the average of normalized scattering angular distributions for 50, 70, and 50 individual soot particles with mobility diameters of 300, 500 and 700 nm, respectively. The APM was not used for the size selection of the soot particles. In the simulations, the RI of the soot particles was assumed to be m =1.95 - 0.79i (Bond and Bergstrom 2006).

For all the particle sizes studied, local minimum values were observed at ~90° for parallel data, while no significant local minimum was observed for perpendicular data (Figs. 6.2, 6.3 and 6.4). The differential scattering cross sections for aggregates can be expressed by the product of Rayleigh-like scattering components and scattering components related to the aggregate structures (Mountain and Mulholland 1988; Weiner et al. 2003; Köylü and Faeth 1994). The Rayleigh-like scattering components result in a minimum at 90° for parallel polarization, but are independent of scattering angle for perpendicular polarization. In contrast, the scattering components of the aggregate structures arise from interference in the far field of the scattering by individual small spherules forming the aggregates. These components do not depend on polarization direction and are considered to decrease monotonically with scattering angle from 0° to 180°, even for different aggregate sizes. The angular distributions observed in the present study are qualitatively consistent with these theoretical predictions (Mountain and Mulholland 1988; Farias et al. 1996) and previously reported angular distributions for soot aggregates (Weiner et al. 2003; Köylü and Faeth 1994; Williams and Hottel

1970).

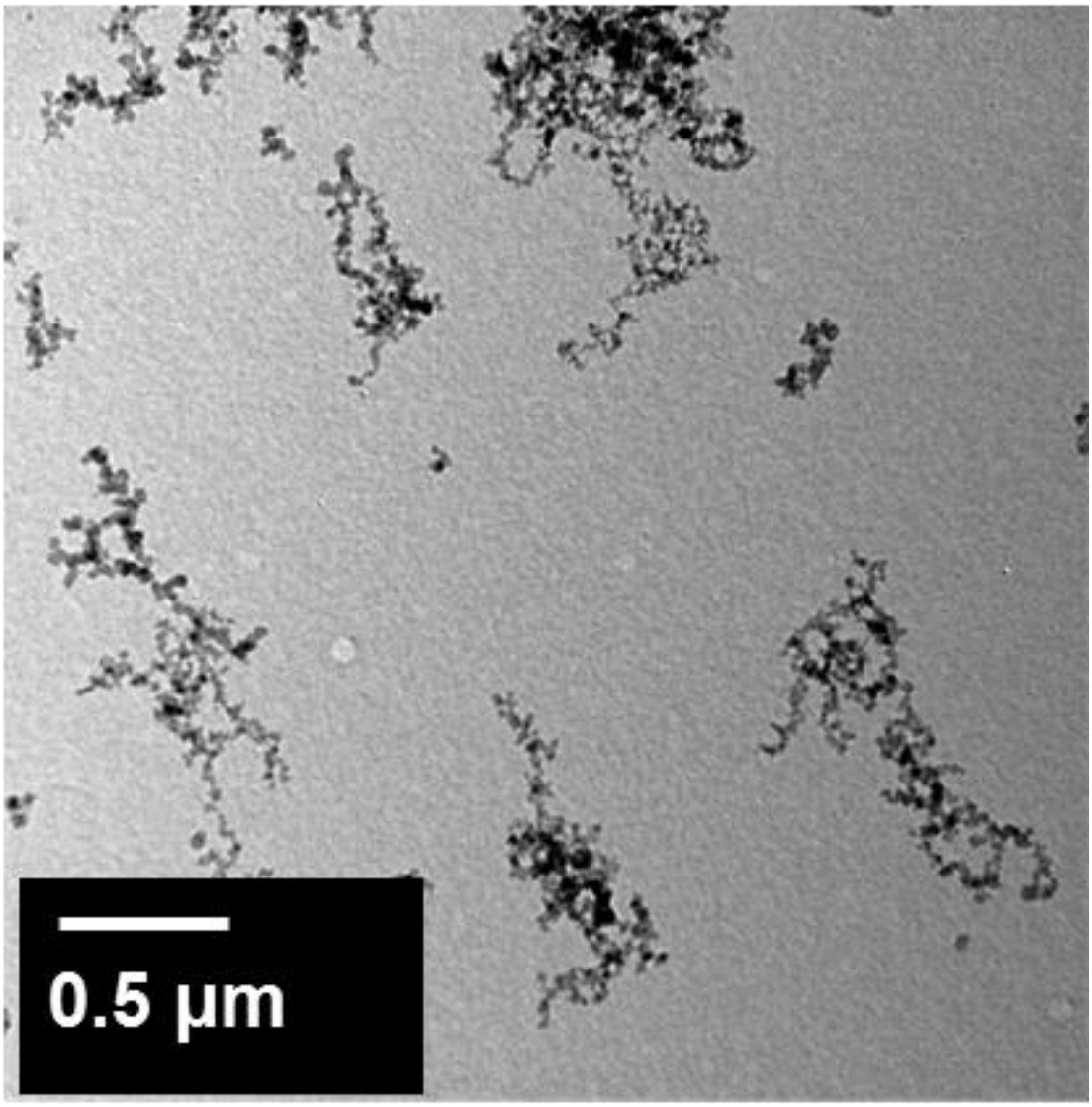

Figure 6.1. TEM images for propane soot particles with mobility diameter of 400 nm.

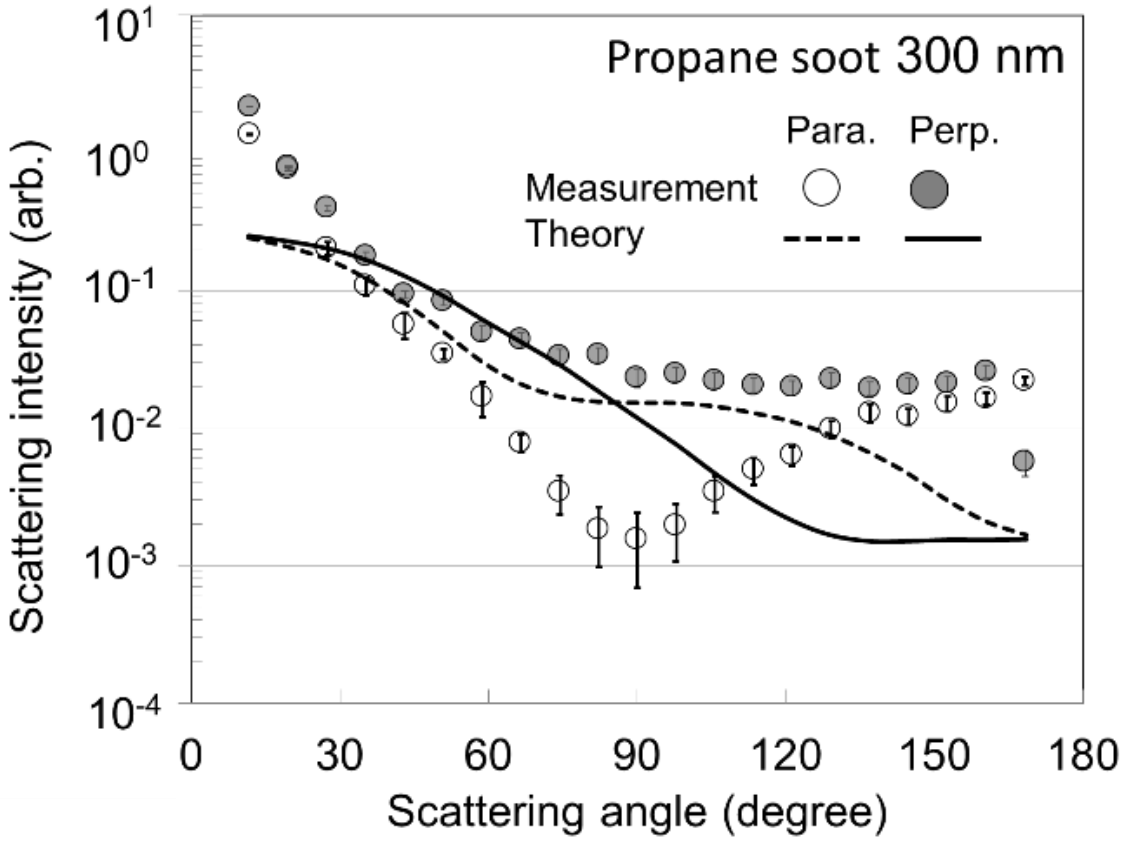

Figure 6.2. Averaged angular distribution of light scattering for incident light polarized parallel (open symbols) and perpendicular (filled symbols) to the scattering plane for propane soot particles with mobility diameters of 300 nm. The error bars indicate the 1σ values for 50 individual particles. The solid and dashed lines represent the results of simulation based on Lorentz-Mie theory assuming spherical particles. Note that the vertical axis has a log scale.

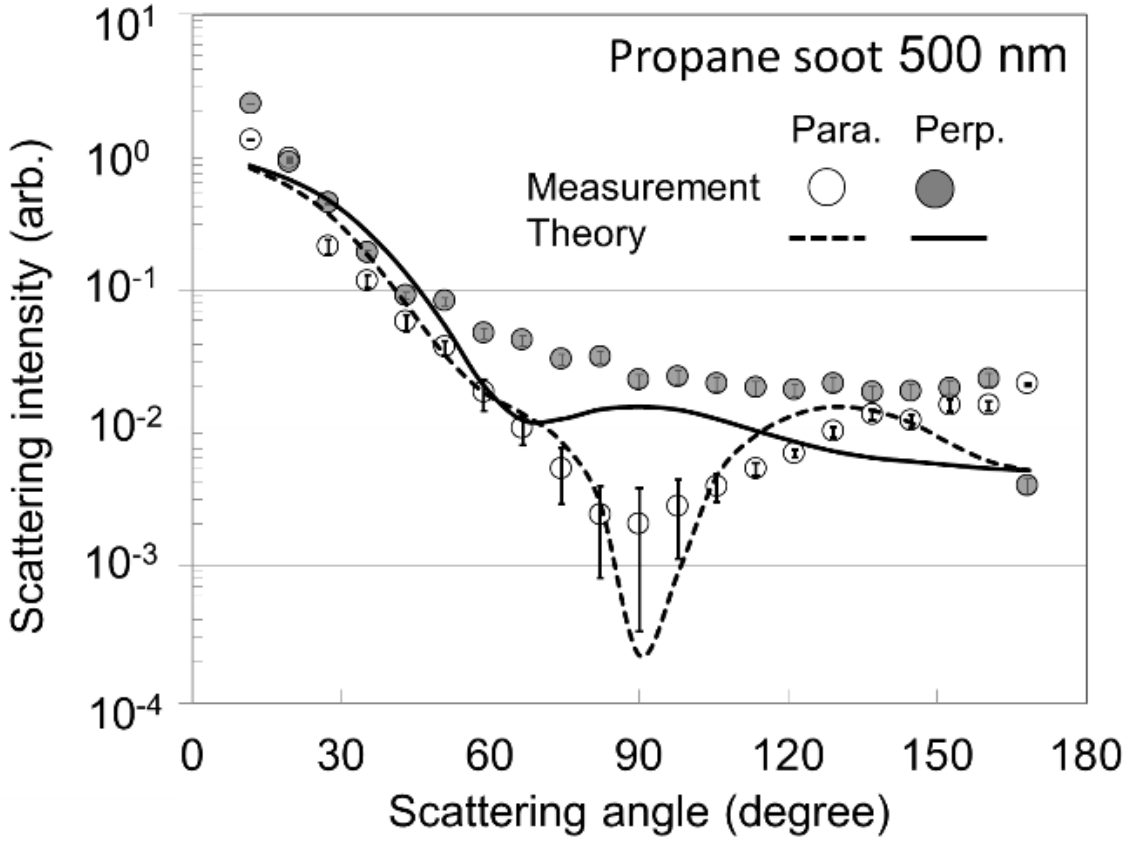

Figure 6.3. The same with Fig. 6.2, but soot particles with mobility diameters of 500 nm and the error bars indicate the 1σ values for 70 individual particles.

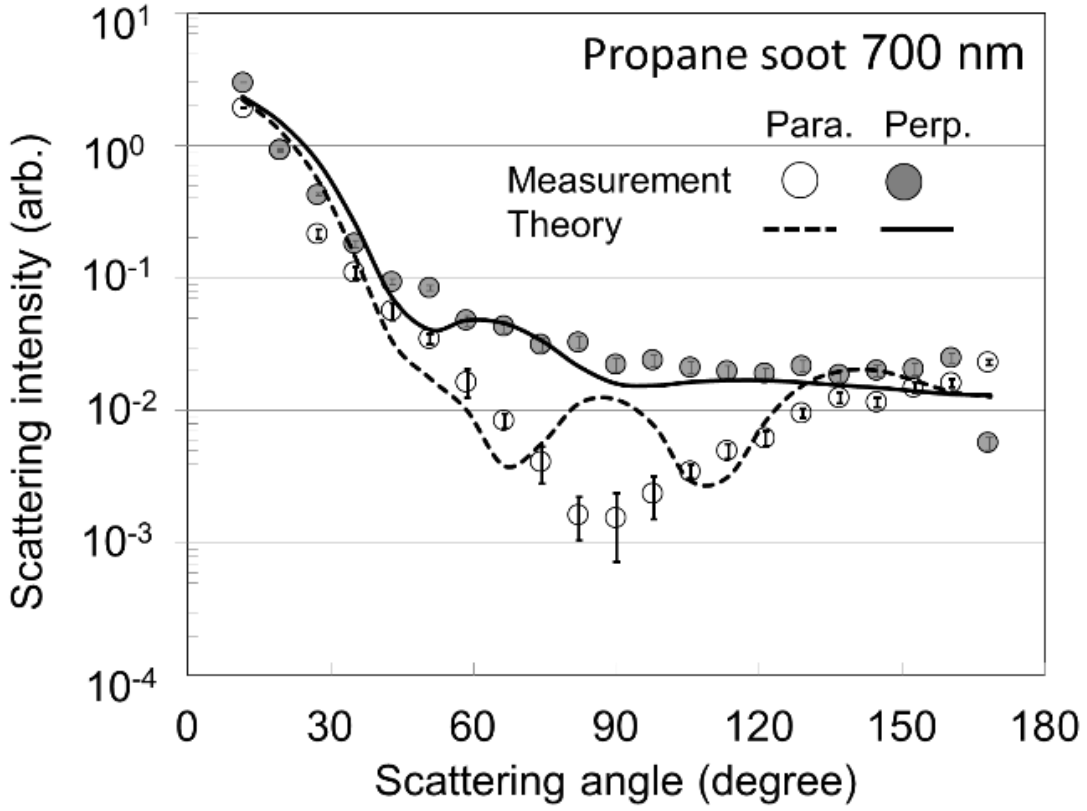

Figure 6.4. The same with Fig. 6.2, but soot particles with mobility diameters of 700 nm and the error bars indicate the 1σ values for 50 individual particles.

Chapter 7

Ambient particles

7.1 Introduction

Measurement of the angular distributions of scattering is applicable to real time monitoring of spherical and non-spherical particles. It is expected that distinguishing between spherical and nonspherical particles should be useful for the understandings of mixing state and origin of particles. Atmospheric aerosol particles consist of inorganic and organic materials. Because of their hygroscopic properties, inorganic salts particles such as ammonium sulfate tend to be near spherical in shape (Sjogren et al. 2007). In contrast, fresh soot particles tend to be non-spherical in shape (Chen et al. 2005). The optical properties of soot depend on the morphological structures (Adler et al. 2010).

Information about the effective density of dry aerosol particles is important to get the mixing state of ambient particles. Nakayama et al. (2014) inferred the effective density distributions of non-refractory particles fell into the range of 1.3 to 1.5 g cm^{-3}, whereas BC particles with an aggregate structure fell into the range of 0.5 to 0.6 g cm^{-3} in an urban site in Nagoya. In this chapter, the scattering properties for ambient particles with different effective densities were investigated.

7.2 Experiment

The details of the PN used in this study are shown in Chapter2. Only a brief description of the ambient particles experiment will be provided here. Ambient particles were measured at the Higashiyama campus of Nagoya University (35°09′N, 136°58′E, 60 m above sea level) located in an urban area in Nagoya, Japan (Nakayama et al. 2014), on February 26, 2014. With a population of 2.3 million, Nagoya is the fourth largest city

in Japan and a strong anthropogenic influence on the sampled particles would be expected. Particles with a mobility diameter of 500 nm and an average effective density of 0.3 or 1.4 g/cm^3 were selected using the DMA and APM after passing through the diffusion dryer, and then introduced into the PN (Fig. 2.8c). The effective density was defined as the ratio of mass to volume based on the DMA-APM technique. The mass and volume component calculated from the mass measured by APM and mobility equivalent diameter measured by DMA, respectively. The effective density of fractal aggregate soot particles is known to be smaller compared to those for spherical particles (Park et al.2003).Sampling periods of particles with average effective densities of 0.3 and 1.4 g/cm^3 were 13:33 to 14:33 and 14:35 to 15:35, respectively. Ambient particles were also collected using the impactor for morphological analysis using the TEM, after passing through the diffusion dryer, DMA and APM.

7.3 Results and discussion

Ambient particles were dried using a diffusion dryer, and their size and effective density of particles were selected using the DMA and APM. Particles with a mobility diameter of 500 nm and an average effective density of 1.4 or 0.3 g/cm^3 were measured using the PN. Particles with average effective density of 1.4 g/cm^3 were considered to be near spherical in shape and mainly consist of inorganic salts and organic matter, whereas those with an average effective density of 0.3 g/cm^3 were considered to be mainly non-spherical particles such as soot (Nakayama et al. 2014). Figures 7.1 and 7.2 show the TEM images for ambient particles with mobility diameter of 500 nm and effective densities of 1.4 and 0.3 g/cm^3, respectively.

Figures 7.3 and 7.4 show histograms of the circularity factor (*CF*) for 376 and 226

individual particles with average effective densities of 1.4 and 0.3 g/cm^3, respectively. Here, $CF = 4\pi A_p/L_p^2$, where A_p and L_p are respectively the projected area and perimeter. The *CF* value for a circle is 1, while the value for irregular shape is less than 1. As can be seen in Fig. 7.1, particles with an average effective density of 0.3 g/cm^3 have smaller *CF* values than those for particles with an average effective density of 1.4 g/cm^3. The mean (median) of the *CF* values for particles with effective densities of 0.3 and 1.4 g/cm^3 were 0.51 (0.52) and 0.60 (0.64), respectively.

Figures 7.5 and 7.6 show averages of normalized angular distributions of scattering for individual ambient particles with a mobility diameter of 500 nm and effective densities of 1.4 or 0.3 g/cm^3. The *n* values for ammonium sulfate and organic matter were reported to be 1.52 and 1.35-1.65, respectively, at 532 nm (Petterson et al. 2004, Moise et al. 2015), while the *k* values for these compounds were typically < 0.01 at 532 nm (Moise et al. 2015, Laskin et al. 2015). Simulations were therefore performed with RI values of m = 1.52 - 0.00i, 1.35 - 0.00i, and 1.65 - 0.00i. A local minimum at a scattering angle of ~70° for perpendicular polarization was observed for particles with an average effective density of 1.4 g/cm^3 (Fig. 7.5). In contrast, no local minimum value at ~70° for perpendicular polarization was seen for particles with an average effective density of 0.3 g/cm^3 (Fig. 7.6). These results were consistent with the results of the TEM analyses of the particles collected after passing through the DMA and APM.

As demonstrated in the present study, combination of the PN with the DMA and/or APM will provide valuable information for the real-time determination of aerosol properties and categorization of the ambient particles. Addition of sensor(s) to measure other scattering parameters, such as azimuthal scattering, forward scattering pattern, and depolarization ratio, would be one of the promising directions for future research.

Although the purpose of the present work is to demonstrate the applicability of our single particle PN for characterizing ambient particles, it should be noted that our PN can be used for the accurate determination of asymmetric parameters (one of the important input parameter for radiative transfer calculations (*e.g.*, Andrews et al. 2006, Horvath et al. 2016)) for individual particles.

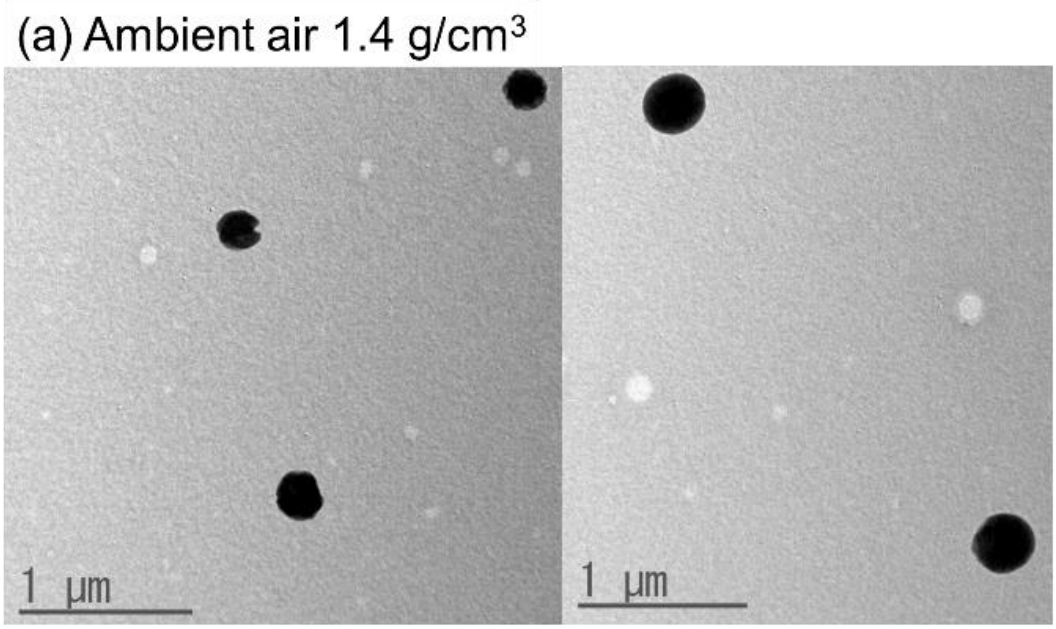

Figure 7.1. TEM images for ambient particles with a mobility diameter of 500 nm and average effective densities of 1.4 g/cm^3.

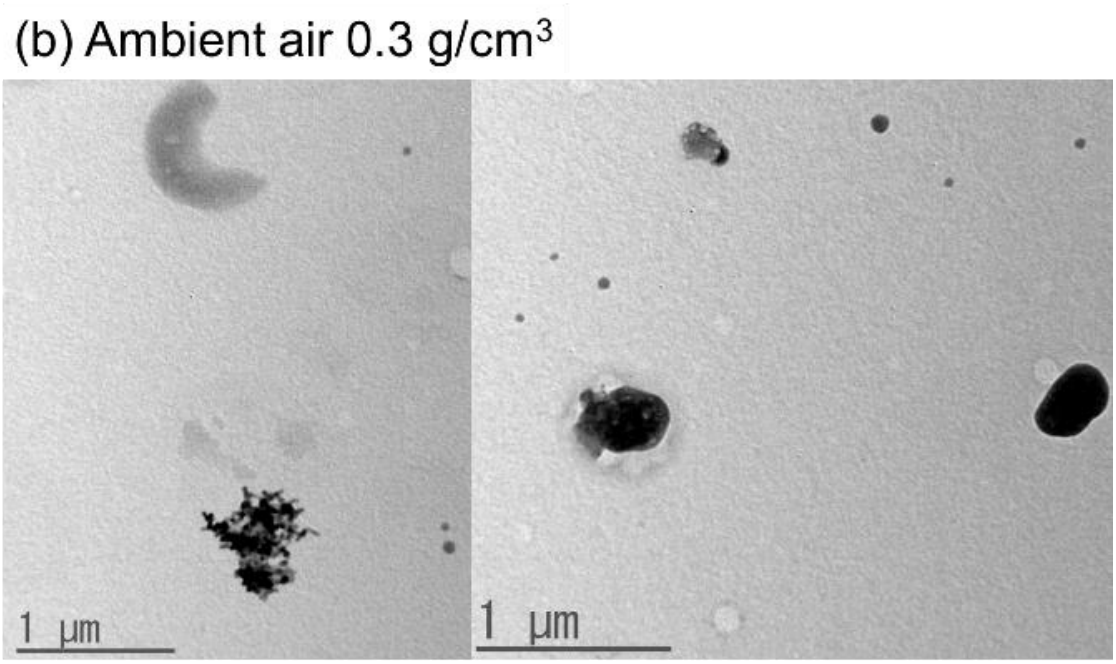

Figure 7.2. The same with Fig. 7.1, but the average effective densities are 0.3 g/cm^3.

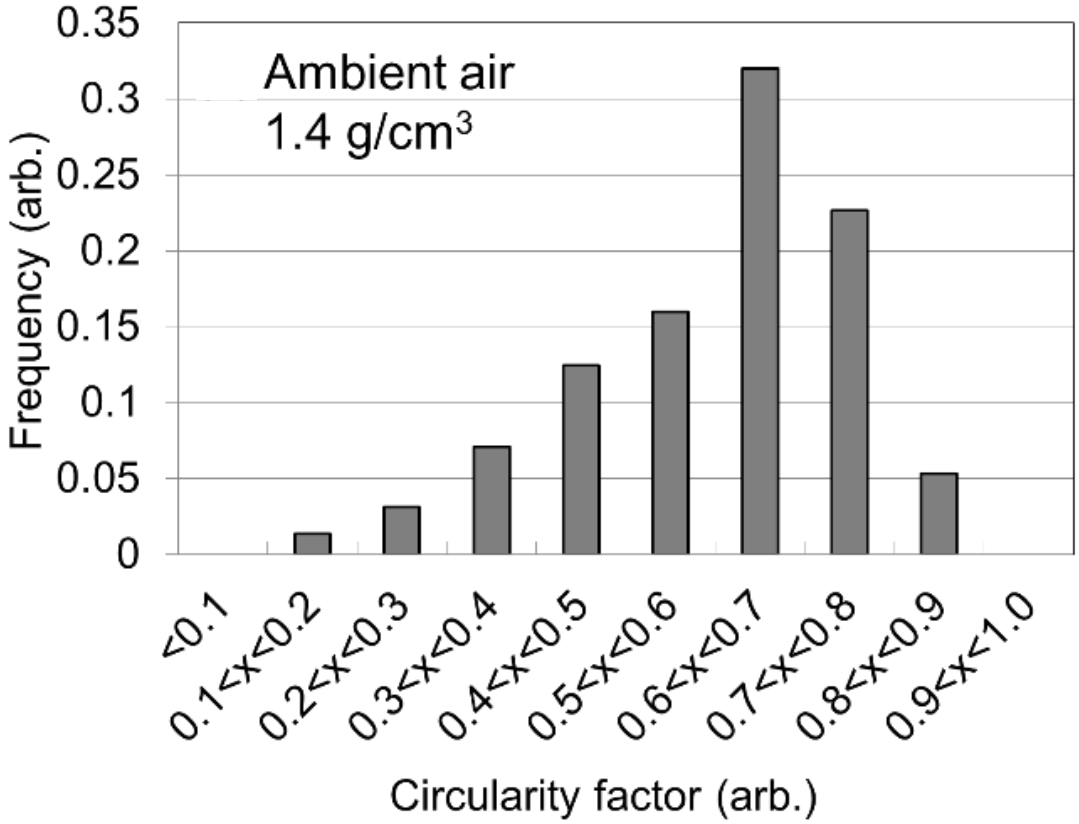

Figure 7.3. Histograms of circularity factor for ambient particles with mobility diameter of 500 nm and average effective density of 1.4 g/cm^3. The CF values for 376 individual particles were analyzed.

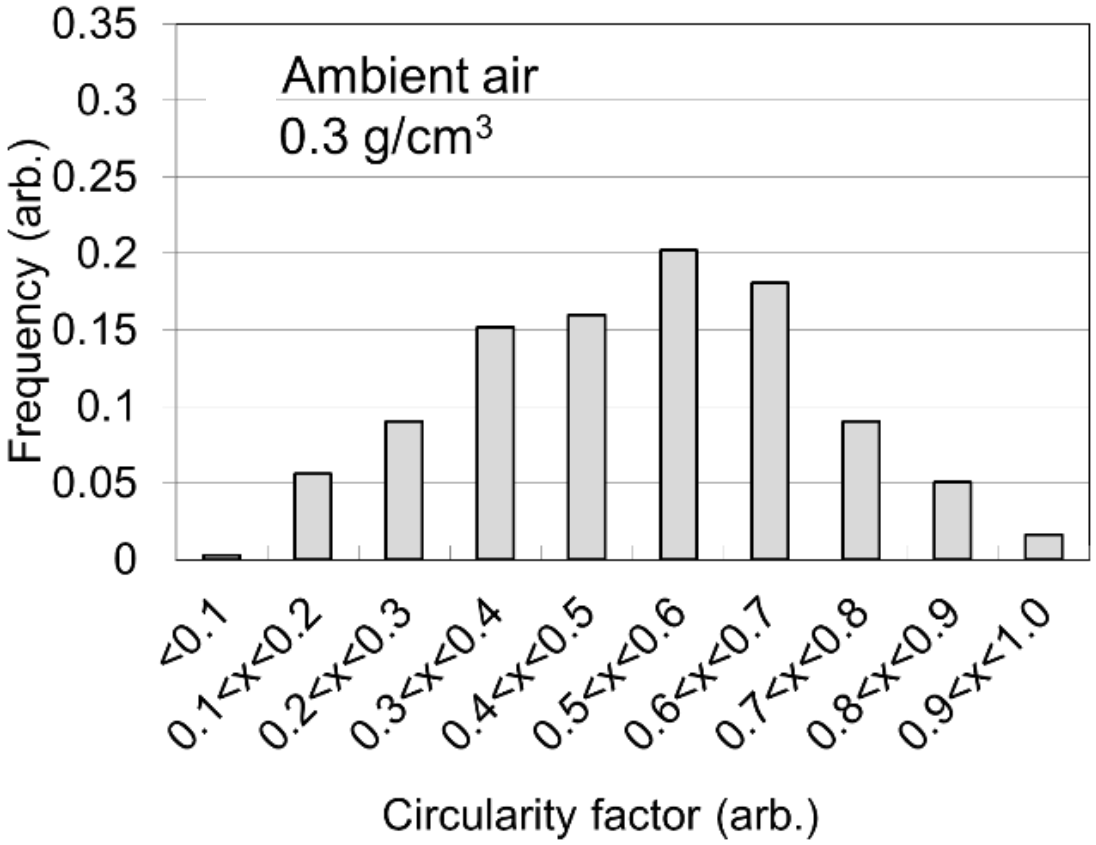

Figure 7.4. The same with Fig. 7.3, but the average effective densities are 0.3 g/cm^3 and the CF values for 226 individual particles were analyzed.

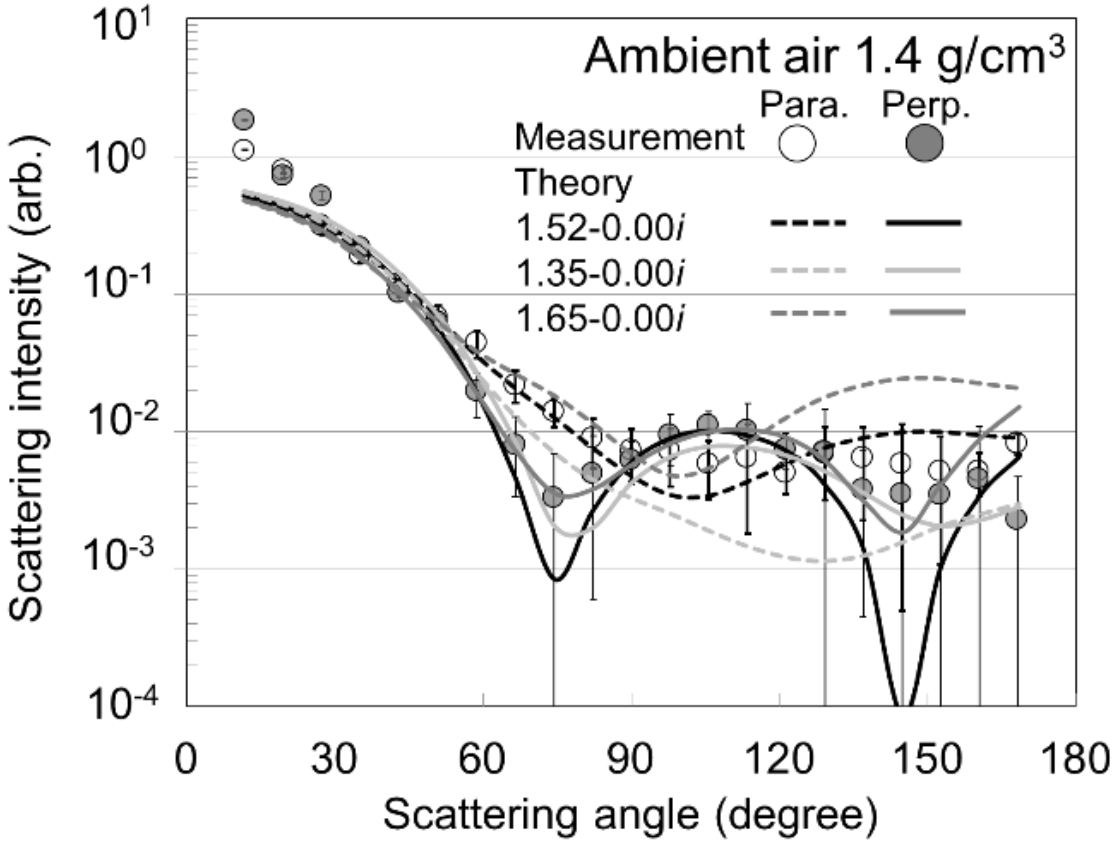

Figure 7.5. Averages of angular distribution of light scattering for incident light polarized parallel (open symbols) and perpendicular (filled symbols) to the scattering plane for individual ambient particles with mobility diameter of 500 nm and an average effective density of 1.4 g/cm^3. The error bars indicate the 1σ values for 42 individual particles. The solid and dashed lines represent the results of simulation based on Lorentz-Mie theory. Note that the vertical axis has a log scale.

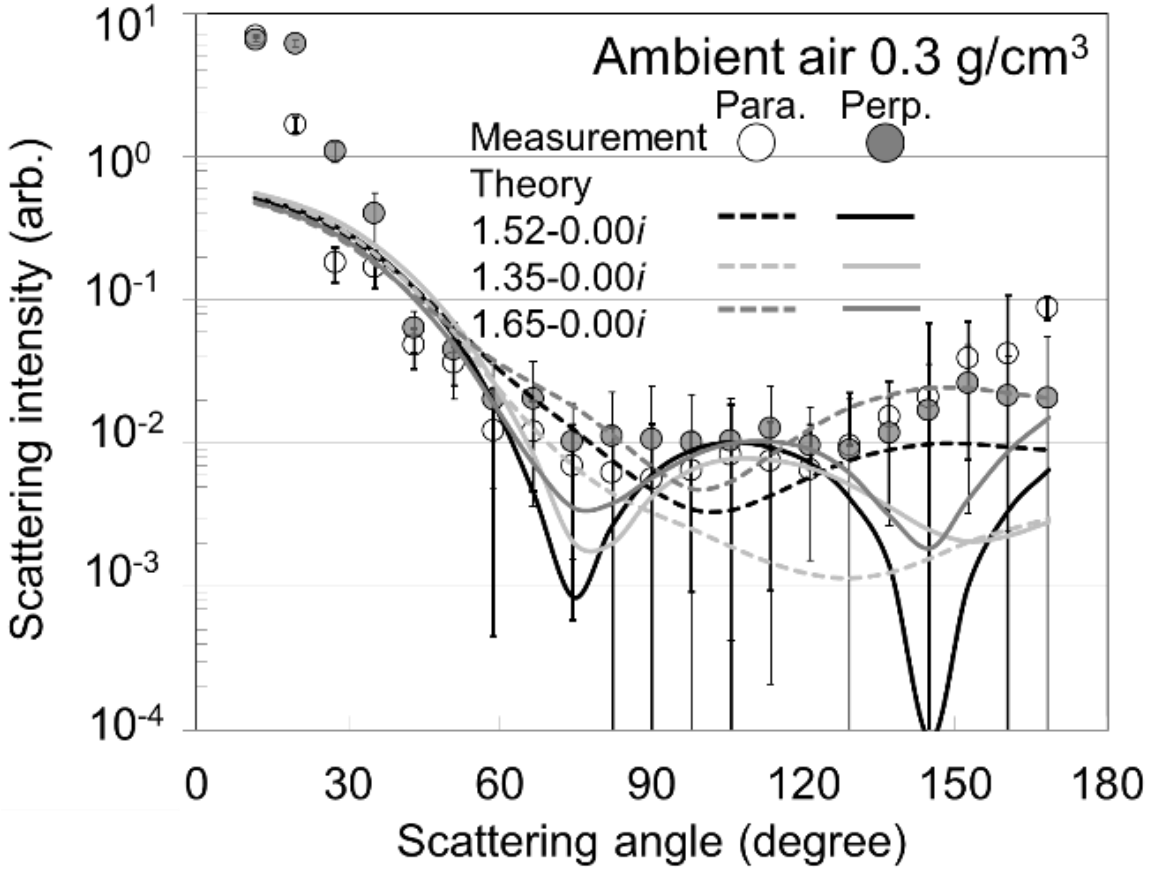

Figure 7.6. The same with Fig. 7.5, but n average effective density of 0.3 g/cm^3 and the error bars indicate the 1σ values for 33 individual particles.

Chapter 8

Summary

This paper describes a new PN designed to achieve real-time measurement of the scattering angular distribution of individual particles. The angular distributions at scattering angle from 11.7° to 168.3° for incident laser light at 532 nm polarized (a) parallel and (b) perpendicular to the scattering plane were simultaneously measured. Laboratory experiments to validate the performance of the instruments were conducted using nearly mono-disperse spherical (PSL and nigrosine) and non-spherical (NaCl and soot) particles.

The observed scattering angular distributions for individual PSL particles with diameters from 299 to 707 nm were in good agreement with the results of simulations based on Lorentz-Mie theory which used literature RI values and accounted for the detection efficiency and angular resolution of each detector. The *n* and *k* values of RI for nigrosine particles with diameters of 300, 500, and 700 nm were determined by comparing the observed scattering angular distributions with the results of simulations. Values for *n* (1.60-1.61) and *k* (0.11-0.14) were consistent among the three diameters.

We also measured scattering angular distributions of non-spherical particles. Differences in the measured and simulated scattering angular distributions were observed for NaCl particles with mobility diameters of 500 and 700 nm, when spherical shape was assumed in the simulations, while good agreement was observed for smaller particles with mobility diameters of 300 nm. These results were reasonably explained by the interference of scattered waves. In the case of soot particles with aggregate structures, similar scattering angular distributions were observed for diameters of 300,

500, and 700 nm with a minimum at 90° (parallel polarization) and a monotonic decrease with increasing scattering angle (perpendicular polarization). These results were also consistent with theoretical predictions for particles with aggregated structures. Our results suggest that our PN can distinguish between spherical and non-spherical particles, especially when the particle diameter is large enough or non-spherical particles have an aggregate structure.

We also conducted test observations of ambient particles at an urban area in Japan. The particles were introduced into the PN after size and effective density selections using the DMA and APM. The local minimum value at scattering angle of ~70° for perpendicular polarization in the scattering angular distribution was observed for particles with an average effective density of 1.4 g/cm^3. In contrast, no local minimum value at a scattering angle of ~70° for perpendicular polarization was observed for particles with an average effective density of 0.3 g/cm^3. Our results suggest that, at least under specific conditions, nearly spherical inorganic salt and organic particles with an average effective density of around 1.4 g/cm^3 are distinguishable from non-spherical particles with an average effective density of around 0.3 g/cm^3 in the atmosphere.

References

Adachi, K., and Buseck, P. R. (2011). Atmospheric Tar Balls from Biomass Burning in Mexico. *Jour. Geophys. Res.: Atmospheres*, **116**:D05204.

Adler, G., Riziq, A. A., Erlick, C., and Rudich, Y. (2010). Effect of Intrinsic Organic Carbon on the Optical Properties of Fresh Diesel Soot. *Proc. Natl. Acad. Sci.*, **107:**6699-6704.

Air Resource Specialists, Inc. (2005). Reevaluation of HFC 134a (SUVA) Span Gas Multiplier.http://vista.cira.colostate.edu/DatawareHouse/IMPROVE/Data/OPTICAL/Nephelometer/NephReprocessing93_04_July2005.doc.

Andrews, E, Sheridan, P. J., Fiebig, M., McComiskey, A., Ogren, J. A., Arnott, P., Covert, D., Elleman, R., Gasparini, R., Collins, D., Jonsson, H., Schmid, B., Wang, J. (2006). Comparison of Methods for Deriving Aerosol Asymmetry Parameter. *J. Geophys. Res.*, **111**:D05S04, doi:10.1029/2004JD005734.

Barkey, B., Paulson, S., and Chung, A. (2007). Genetic Algorithm Inversion of Dual Polarization Polar Nephelometer Data to Determine Aerosol Refractive Index. *Aerosol Sci. Technol.*, **41**:751–760.

Barkey, B., Paulson, S., and Liou, K. N. (2012). Polar Nephelometers for Light Scattering by Ice Crystals and Aerosols: Design and Measurements. *Light Scattering Reviews*, **6**:3-37.

Bohren, C. F. and Huffman, D. K. (1983). A*bsorption and Scattering of Light by Small Particles*.Wiley, New York.

Bohren, C. F. and Clothiaux, E. E. (2006). *Fundamentals of Atmospheric Radiation: An Introduction with 400 Problems*. Wiley, New York.

Bond, T. C., and Bergstrom, R. W. (2006). Light Absorption by Carbonaceous

Particles: An Investigative Review. *Aerosol Sci. Technol*., **40**:27–67.

Boucher, O. *et al.* (2013). Clouds and Aerosols. In T. F. Stocker et al. (eds.): *Climate Change 2013: The Physical Science Basis. Contribution of Working Group I to the Fifth Assessment Report of the Intergovernmental Panel on Climate Change*. Cambridge University Press, Cambridge, United Kingdom and New York, NY, USA.

Chamberlain-Ward, S. and Sharp, F. (2011). Advances in Nephelometry through the Ecotech Aurora Nephelometer. *The Scientific World JOURNAL*, **11**:2530–2535.

Chen Y. Z., Shah N, Huggins F. E., and Huffman G. P. (2005). Transmission Electron Microscopy Investigation of Ultrafine Coal Fly Ash Particles. *Environ Sci Technol*, **39**:1144–51.

Dalzell, W. H., Williams, G. C., and Hottel, H. C. (1970). A Light-Scattering Method for Soot Concentration Measurements. *Combustion and Flame*, **14**:161-169.

Dick, W. D. and McMurry, P. H. (2007). Multiangle Light-Scattering Measurements of Refractive Index of Submicron Atmospheric Particles. *Aerosol Sci. Technol*., **41**:549–569.

Dinar, E., Riziq, A. A., Spindler, C., Erlick, C., Kiss, G., and Rudich, Y. (2008). The Complex Refractive Index of Atmospheric and Model Humic-Like Substances (HULIS) Retrieved by a Cavity Ring Down Aerosol Spectrometer (CRD-AS). *Faraday Discuss*., **137**:279–295.

Farias, T. L., Köylü, Ü. Ö., Carvalho, M. G. (1996). Effects of Polydispersity of Aggregates and Primary Particles on Radiative Properties of Simulated Soot. *J. Quant. Spectrosc. Radiat. Trans.*, **55**:357-371.

Flores, J. M., Bar-Or, R. Z., Bluvshtein, N., Abo-Riziq, A., Kostinski, A., Borrmann, S., Koren, I., Koren, I., and Rudich, Y. (2012). Absorbing Aerosols at High Relative

Humidity: Linking Hygroscopic Growth to Optical Properties. *Atmos. Chem. Phys.*, **12**:5511–5521.

Garvey, D. M. and Pinnick, R. G. (1983). Response Characteristics of the Particle Measuring Systems Active Scattering Aerosol Spectrometer Probe (ASASP-X). *Aerosol Sci. Technol*., **2**:477–488.

Guo, X., Nakayama, T., Yamada, H., Inomata, S., Tonokura, K., and Matsumi, Y. (2014). Measurement of the Light Absorbing Properties of Diesel Exhaust Particles Using a Three-Wavelength Photoacoustic Spectrometer. *Atmos. Environ.*, **94**:428–437.

Hansen, M. Z. and Evans, W. H. (1980). Polar nephelometer for Atmospheric Particulate Studies. *Applied optics.*, **19**:3389-3395.

Hoffer, A., Tóth, A., Nyirő-Kósa, I., Pósfai, M., and Gelencsér, A. (2016). Light Absorption Properties of Laboratory-Generated Tar Ball Particles. *Atmos Chem and Phys.*, **16**:239-246.

Horvath, H., Kasahara, M., Tohno, S., Olmo, F. J., Lyamani, H., Alados-Arboledas, L., Quirantes, A., Cachorro, V. (2016). Relationship between Fraction of Backscattered Light and Asymmetry Parameter. *J. Aerosol Sci.*, **91**:43-53.

Kim, H. and Paulson, S. E. (2013). Real Refractive Indices and Volatility of Secondary Organic Aerosol Generated from Photooxidation and Ozonolysis of Limonene, α-pinene and Toluene. *Atmos. Chem. Phys*., **13**:7711-7723.

Kim, H., Kim, J. Y., Kim, J. S., & Jin, H. C. (2015). Physicochemical and Optical Properties of Combustion-Generated Particles from a Coal-Fired Power Plant, Automobiles, Ship Engines, and Charcoal Kilns. *Fuel*, **161**:120-128.

Köylü, U. O. and Faeth, G. M. (1994). Optical Properties of Overfire Soot in Buoyant

Turbulent Diffusion Flames at Long Residence Times. *J. Heat Trans.*, **116**:152-159.

Krauth, W. (2006). *Statistical Mechanics: Algorithms and Computations*, Oxford University Press, Oxford.

Lack, D. A., Lovejoy, E. R., Baynard, T., Pettersson, A., and Ravishankara, A. R. (2006). Aerosol Absorption Measurement Using Photoacoustic Spectroscopy: Sensitivity, Calibration, and Uncertainty Developments. *Aerosol Sci. Technol.*, **40**:697–708.

Lang-Yona, M., Rudich, Y., Segre, E., Dinar, E., and Abo-Riziq, A. (2009). Complex Refractive Indices of Aerosols Retrieved by Continuous Wave-Cavity Ring Down Aerosol Spectrometer. *Anal. Chem.*, **81**:1762–1769.

Laskin, A., Laskin, J., and Nizkorodov, S. A. (2015). Chemistry of Atmospheric Brown Carbon. *Chem Rev*., **115**:4335-4382.

Liu, P. F., Zhang, Y., and Martin, S. T. (2013). Complex Refractive Indices of Thin Films of Secondary Organic Materials by Spectroscopic Ellipsometry from 220 to 1200 nm, *Environ. Sci. Technol.*, **47**:13594–13601.

Mackowski, D. W. (2013). MSTM – a Multiple Sphere T-matrix FORTRAN Code for Use on Parallel Computer Clusters, Department of Mechanical Engineering, Auburn University, Auburn, AL 36849, USA, available at: http://eng.auburn.edu/users/dmckwski/scatcodes.

McCrowey, C. J., Tinilau, S. S., Calderon, G., Koo, J. -E., and Curtis, D. B. (2013). A portable High-Resolution Polar Nephelometer for Measurement of the Angular Scattering Properties of Atmospheric Aerosol: Design and Validation. *Aerosol Sci. Technol*.,**47**:592–605.

McMurry, P. H. (2000). A Review of Atmospheric Aerosol Measurements. *Atmos*

Environ, **34**:1959-1999.

Moise, T., Flores, J. M., and Rudich, Y. (2015). Optical Properties of Secondary Organic Aerosols and Their Changes by Chemical Processes. *Chem. Rev*., **115**:4400–4439.

Moosmüller, H., Chakrabarty, R. K., and Arnott, W. P. (2009). Aerosol Light Absorption and Its Measurement: A Review. *J. Quant. Spectrosc. Radiat. Trans.*, **110**:844-878.

Mountain, R.D., and Mulholland, G.W. (1988). Light Scattering from Simulated Smoke Agglomerates. *Langmuir*, **4**:1321-1326.

Nakayama, T., Kondo, Y., Moteki, N., Sahu, L. K., Kinase, T., Kita, K., and Matsumi, Y. (2010). Size-Dependent Correction Factors for Absorption Measurements Using Filter-Based Photometers: PSAP and COSMOS. *J. Aerosol Sci*., **41**:333–343.

Nakayama, T., Ikeda, Y., Sawada, Y., Setoguchi, Y., Ogawa, S., Kawana, K., Mochida, M., Ikemori, F., Matsumoto, K., and Matsumi, Y. (2014). Properties of Light-Absorbing Aerosols in the Nagoya Urban Area, Japan, in August 2011 and January 2012: Contributions of Brown Carbon and Lensing Effect. *J. Geophys. Res. Atmos.*, **119**:12721–12739.

Nakayama, T., Suzuki, H., Kagamitani, S., Ikeda, Y., Uchiyama, A., and Matsumi, Y. (2015). Characterization of a Three Wavelength Photoacoustic Soot Spectrometer (PASS-3) and a Photoacoustic Extinctiometer (PAX). *J. Meteorol. Soc. Jpn.*, **93**, 285–308.

Nikolov, I. D. and Ivanov, C. D. (2000). Optical Plastic Refractive Measurements in the Visible and the Near-Infrared Regions. *Appl. Opt*., **39**:2067–2070.

Park, K., Cao, F., Kittelson, D. B., and McMurry, P. H. (2003). Relationship between Particle Mass and Mobility for Diesel Exhaust Particles. *Environ. Sci. Technol.*, **37**:577-583.

Perry, R. J., Hunt, A. J., and Huffman, D. R. (1978). Experimental Determinations of Mueller Scattering Matrices for Nonspherical Particles. *Appl. Opt.*, **17**:2700–2710.

Pettersson, A., Lovejoy, E. R., Brock, C. A., Brown, S. S., and Ravishankara, A. R. (2004). Measurement of Aerosol Optical Extinction at 532 nm with Pulsed Cavity Ring Down Spectroscopy. *J. Aerosol. Sci*., **35**:995–1011.

Pinnick, R. G., Carroll, D. E., and Hofmann, D. J. (1976). Polarized light scattered from monodisperse randomly oriented nonspherical aerosol particles: measurements. *Appl. Opt.*, **15**:384-393.

Pinnick, R. G., and Auvermann, H. J. (1979). Response Characteristics of Knollenberg Light-Scattering Aerosol Counters. *J. Aerosol Sci.*, **10**:55–74.

Radney, J. G., You, R., Ma, X., Conny, J. M., Zachariah, M. R., Hodges, J. T., and Zangmeister, C. D. (2014). Dependence of Soot Optical Properties on Particle Morphology: Measurements and Model Comparisons. *Env. Sci. Tech.,* **48**:3169-3176.

Sachweh, B. A., Dick, W. D., and McMurry, P. H. (1995). Distinguishing between Spherical and Nonspherical Particles by Measuring the Variability in Azimuthal Light Scattering. *Aerosol Sci. Technol.,* **23**:373–391.

Schmitt, C. A. (1944). The Chemistry of Writing Inks. *J. Chem. Educ.*, **21**:413.

Sjogren, S., Gysel, M., Weingartner, E., Baltensperger, U., Cubison, M. J., Coe, H. Zardini. A.A., Marcollic, C., Kriegerc, U.K., and Peter, T. (2007). Hygroscopic Growth and Water Uptake Kinetics of Two-Phase Aerosol Particles Consisting of Ammonium sulfate, Adipic and Humic Acid Mixtures. *Jour. Aerosol Sci.*, **38**:157-171.

Tajima, N., Fukushima, N., Ehara, K., and Sakurai, H. (2011). Mass Range and Optimized Operation of the Aerosol Particle Mass Analyser. *Aerosol Sci.Technol.*,

45:196–214.

Volten, H., Munoz, O., Rol, E., de Haan, J., Vassen, W., Hovenier, J., Muinonen, K., and Nousiainen, T. (2001). Scattering Matrices of Mineral Aerosol Particles at 441.6 nm and 632.8 nm. *J. Geophys. Res.*, **106**:17375–17401.

Weinert, D., Cleary, T. G., Mulholland, G. W., and Beever, P. (2003). Light Scattering Characteristics and Size Distribution of Smoke and Nuisance Aerosols. *Fire Safety Sci.*, **7**:209-220.

Whitby, K. T., and Liu, B. Y. (1968). Polystyrene Aerosols—Electrical Charge and Residue Size Distribution. *Atmos Environ.*, **2**:103-116.

Woo, C. G., You, S., and Lee, J. (2013). Determination of Refractive Index for Absorbing Spheres. *Optik-International Journal for Light and Electron Optics.*, **124**:5254-5258.

Wyatt, P. J., Schehrer, K. L., Philips, S. D., Jackson, C., Chang, Y. J., Parker, R. G., Phillips, D. T., and Bottiger, J. R. (1988). Aerosol Particle Analyzer. *Appl. Opt.*, **27**:217–221.

Xue, H., Khalizov, A. F., Wang, L., Zheng, J. Zhang, R. (2009). Effects of Coating of Dicarboxylic Acids on the Mass-Mobility Relationship of Soot Particles. *Environ. Sci. Technol.*, **43**:2787-2792.

Yurkin, M. A. and A. G. Hoekstra. (2007). The Discrete Dipole Approximation: An Overview and Recent Developments. *J. Quant. Spectrosc. Radiat. Trans.*, **106**:558-589.

Acknowledgements

The present work was carried out at the Institute for Space-Earth Environmental Research (ISEE) and Graduate School of Science, Nagoya University and I would like to thank the people who help me a lot for their cooperation in carrying out this study.

Foremost, the author would like to thank Prof. Yutaka Matsumi (Nagoya Univ.) for technical assistance with the experiments. The authors are grateful to Prof. Matsumi for suggesting the topic treated in this paper and for providing adequate guidance. I am also very grateful to a lecturer Tomoki Nakayama (Nagoya Univ.) for most helpful advice and discussions, who helped me with the experiments.

The author thanks the technical staff of Matsumi laboratory; Mr. Hiroshi Sasago (Nagoya Univ.) for their technical support. The author is grateful to Dr. Sayako Ueda (Nagoya Univ.) for lending their expertise on the application of transmittance electron microscope techniques. I am grateful to Prof. Dean S. Venables (University College Cork) for insightful comments and suggestions for this work. I would like to thank the members of Department of Chemistry and Environmental Research Institute at University College Cork for their hospitality during my visit. The author would like to thank the technical staffs of ISEE; Noriji Toriyama (Nagoya Univ.) and Ryuji Fujimori (Nagoya Univ.) Prof. Akira Mizuno and Takashi Shibata (Nagoya Univ.) gave insightful comments and suggestions as Member of Screening Committee.

The author has had the support and encouragement of Japan Association of Aerosol Science and Technology, Japan Society of Atmospheric Chemistry, Japan Geoscience Union and Third symposium on applications of advanced measurement technologies. I would also like to express my gratitude to Nagoya University program for leading

graduate schools, Iwadare Scholarship Foundation and The SanDisk Scholars Program for their financial support.

Without all the members of Matsumi laboratory guidance and persistent help this thesis would not have been possible.

Finally I would like to extend my indebtedness to my family for their endless love, understanding, support, encouragement and sacrifice throughout my study.